Title

Mesophasic organization of GABAA receptors in hippocampal inhibitory synapses

Permalink

Journal

ISSN

Authors

Liu, Yun-Tao
Tao, Chang-Lu
Zhang, Xiaokang
et al.

Publication Date

DOI

Peer reviewed

Mesophasic organization of GABA_A receptors in hippocampal inhibitory synapses

Yun-Tao Liu[1,2,3,8], **Chang-Lu Tao**[1,2,4,8], **Xiaokang Zhang**[4,8], **Wenjun Xia**[5], **Dong-Qing Shi**[2], **Lei Qi**[2], **Cheng Xu**[1], **Rong Sun**[1], **Xiao-Wei Li**[1], **Pak-Ming Lau**[2,4,✉], **Z. Hong Zhou**[3,6,✉], **Guo-Qiang Bi**[1,2,4,7,✉]

[1]Center for Integrative Imaging, Hefei National Laboratory for Physical Sciences at the Microscale, University of Science and Technology of China, Hefei, China.

[2]CAS Key Laboratory of Brain Function and Disease, School of Life Sciences, Division of Life Sciences and Medicine, University of Science and Technology of China, Hefei, China.

[3]California NanoSystems Institute, University of California, Los Angeles, Los Angeles, CA, USA.

[4]Interdisciplinary Center for Brain Information, The Brain Cognition and Brain Disease Institute, Shenzhen Institutes of Advanced Technology, Chinese Academy of Sciences; Shenzhen-Hong Kong Institute of Brain Science-Shenzhen Fundamental Research Institutions, Shenzhen, China.

[5]School of Mathematical Sciences, Jiangsu University, Zhenjiang, China.

[6]Department of Microbiology, Immunology and Molecular Genetics, University of California, Los Angeles, Los Angeles, CA, USA.

[7]CAS Center for Excellence in Brain Science and Intelligence Technology, Chinese Academy of Sciences, Shanghai, China.

[8]These authors contributed equally: Yun-Tao Liu, Chang-Lu Tao, Xiaokang Zhang.

Abstract

Information processing in the brain depends on specialized organization of neurotransmitter receptors and scaffolding proteins within the postsynaptic density. However, how these molecules are organized in situ remains largely unknown. In this study, template-free classification of

oversampled sub-tomograms was used to analyze cryo-electron tomograms of hippocampal synapses. We identified type-A GABA receptors (GABA$_A$Rs) in inhibitory synapses and determined their in situ structure at 19-Å resolution. These receptors are organized hierarchically: from GABA$_A$R super-complexes with a preferred inter-receptor distance of 11 nm but variable relative angles, through semi-ordered, two-dimensional receptor networks with reduced Voronoi entropy, to mesophasic assembly with a sharp phase boundary. These assemblies likely form via interactions among postsynaptic scaffolding proteins and receptors and align with putative presynaptic vesicle release sites. Such mesophasic self-organization might allow synapses to achieve a 'Goldilocks' state, striking a balance between stability and flexibility and enabling plasticity in information processing.

Neuronal synapses are intricate communication devices, operating as fundamental building blocks underlying virtually all brain functions[1-4]. An essential part of the synapse is the lipid-bound, proteinaceous postsynaptic density (PSD), in which neurotransmitter receptors and other synaptic proteins are concentrated[5-8]. The specialized organization of PSD is critical for the efficacy of synaptic transmission[9,10]. Meanwhile, the reorganization of receptors and other PSD proteins is widely known as a mechanism of synaptic plasticity, which, in turn, underlies many cognitive functions, such as learning and memory[11,12].

Different forms of PSD organization have been proposed, including meshwork based on electron microscopy (EM) and biochemical assays[13-15], nano-domains based on super-resolution optical imaging[9,10,16-18] and liquid condensate based on in vitro PSD mixing assay[19,20]. However, the PSD is heterogeneous and pleomorphic, and its protein components are small in size, presenting considerable challenges for resolving its molecular organization. For example, even super-resolution optical imaging can only describe synaptic organizations at the precision of protein clusters with its ~20-nm resolution[16,17,21]. EM, although with higher resolution, lacks molecular specificity, thus hindering the ability to identify synaptic receptors and other proteins inside synapses. These synaptic molecules, such as GABA$_A$Rs, are often small and surrounded by the crowded cellular environment. Consequently, how individual PSD molecules are organized in situ is largely unknown, limiting understanding of molecular mechanisms underlying synaptic formation and functions.

In this study, we employed the state-of-the-art cryo-electron tomography (cryoET) with Volta phase plate and direct electron detector to obtain structures of neuronal synapses in their native conditions. To automatically identify neurotransmitter receptors inside synapses without the need of labeling, we developed a method of template-free classification with uniformly oversampled sub-tomograms on the membrane. With this method, we obtained an in situ structure of GABA$_A$R at 19-Å resolution and discovered a hierarchical organization of GABA$_A$Rs within the PSD, establishing the structural basis for synaptic transmission and plasticity.

Results

Identification of GABA$_A$Rs by oversampling and template-free classification.

To understand the molecular organization of GABA$_A$Rs in situ, we imaged synapses of cultured hippocampal neurons using cryoET with Volta phase plate (Supplementary Video 1). Taking advantage of correlative microscopy, we showed that a thin, sheet-like density parallel to the postsynaptic membrane is a defining feature of GABAergic inhibitory synapses (Fig. 1a), differing from excitatory synapses with much thicker PSDs[7]. Based on this criterion, we identified 72 inhibitory synapses with thin, sheet-like PSDs from 500 high-resolution tomograms acquired without correlative microscopy. Many particles visualized on the postsynaptic membranes in all these synapses have shapes characteristic of pentameric GABA$_A$R[22] (Fig. 1b-e and Supplementary Video 2), which is the most abundant membrane protein species in GABAergic synapses[23,24] (Extended Data Fig. 1 and Supplementary Table 1). We thus assigned these particles as GABA$_A$Rs on the native postsynaptic membranes.

To automate the unbiased identification of GABA$_A$Rs in those inhibitory synapses, we devised a systematic approach that uses oversampling of sub-tomograms to ensure inclusion of all particles existing on the postsynaptic membranes and then classified the oversampled sub-tomograms with a template-free, Bayesian three-dimensional (3D) classification method as implemented in Relion[25] to sort out GABA$_A$R particles from all the particles (Extended Data Figs. 2-4). The structure of GABA$_A$R emerged during the iterative classification (Extended Data Fig. 2c). After eliminating duplicates, we sorted out 9,618 GABA$_A$Rs from all 72 synapses (Extended Data Fig. 2b and Supplementary Table 2) and placed them back on the postsynaptic membranes to visualize their spatial distribution (Fig. 1d). After 3D refinement, a sub-tomogram average of in situ GABA$_A$R was obtained at 19-Å resolution (Fig. 1f,g).

In situ structure of GABA$_A$R.

The sub-tomogram average of GABA$_A$R was ~11 nm in length and ~7 nm in width, with a central vestibule in extracellular domains (Fig. 1f and Extended Data Fig. 5). Overall, our in situ structure matched the previously characterized structure of reconstituted GABA$_A$R[22], except that extra densities were found at the edges of the extracellular domain (Fig. 1f). These extra densities might represent additional glycans[26], and auxiliary proteins or adhesion molecules existed in the native environments[27,28]. Densities for the membrane bilayer were also well resolved (Fig. 1f and Extended Data Fig. 5b). The rough shape of the density for the transmembrane helices matched the atomic models of the reconstituted GABA$_A$Rs[22,26,29-31], with some slight difference that could be due to averaging of different subunits (Fig. 1f and Extended Data Fig. 5a). The intracellular loops (~500 aA, for five subunits, missing in atomic structures) were not observed in our reconstruction even at low threshold (Extended Data Fig. 5b,c), suggesting that those loops are intrinsically flexible even though they are likely to bind to postsynaptic scaffolding proteins in situ.

Super-complex of GABA$_A$Rs.

With the GABA$_A$Rs identified in situ, we next investigated their spatial organization on the postsynaptic membrane. By measuring the distance of each receptor to its neighbors, we

found that the distributions of the first and the second nearest-neighbor (NN) distances both peaked sharply at ~11 nm (Fig. 2a,b), indicating that GABA$_A$Rs tend to maintain a preferred distance with their neighboring receptors. Receptor concentration, measured as the number of receptors per μm$_2$ within the concentric rings around GABA$_A$Rs, also peaked at ~11 nm (Fig. 2c), further supporting that 11 nm is a characteristic inter-receptor distance (IRD). At this distance, the concentration of GABA$_A$R reached ~4,000 μm^{-2}, which was about twice of the plateau level that occurs just 5 nm away (Fig. 2c). This characteristic 11-nm IRD was consistently found in most (64 of 72) synapses (Fig. 2d). The rest had generally fewer receptors and larger median IRDs (Fig. 2d), probably owing to their immaturity in early synapse development. By selecting receptors and their neighboring receptors with 11 ± 4-nm IRDs (Fig. 2e), we obtained a sub-tomogram average of GABA$_A$R super-complex consisting of a pair of receptors (Fig. 2f). Moreover, classification of oversampled sub-tomograms without symmetry also yielded a class with a pair of receptor-like particles with ~11-nm IRD (Extended Data Fig. 5d,e). Thus, this IRD imposes a stringent constraint on the organization of GABA$_A$Rs on the inhibitory postsynaptic membrane. In the averaged receptor pair super-complex, the pseudo five-fold symmetry in both receptors was lost, suggesting that the relative rotation of each receptor was less constrained (Fig. 2f). Indeed, the distribution of the in-plane rotation angle (denoted as angle ω) of a receptor relative to the receptor pair axis was quite uniform (Fig. 2g). Reconstructing the receptor pairs with specific ω angles clearly restored the pseudo five-fold symmetry of the corresponding receptors (Fig. 2h).

One GABA$_A$R could also pair with two other receptors, forming a receptor triplet (Fig. 2e,i). In the triplet structure, whereas the distances between the neighboring receptors were constrained to ~11 nm, the angle (denoted as angle θ) between the two arms of the triplet was unrestricted, with a rather uniform distribution ranging from 60° to 180° (Fig. 2i). The structures of receptor triplets with different θ angles could also be reconstructed (Fig. 2j). Thus, the near-neighbor organization of GABA$_A$Rs is morphologically flexible with variable ω or θ angles but topologically invariable with preferred IRD. This unique feature is characteristic of a mesophasic state, which is neither liquid that does not maintain inter-molecule distance nor crystalline that has constant crystal angles.

Two-dimensional networks of GABA$_A$Rs.

In addition to pairs and triplets of 'linked' receptors, many receptors (26.1%), in fact, had more than two 11-nm neighbors (Fig. 3a) and further organized into two-dimensional (2D) networks of various sizes (Fig. 3b). In the meantime, 20.0% of receptors did not integrate into the network—hereafter defined as solitary receptors (Fig. 3a,b). The proportion of solitary receptors and mean size of the networks were independent of postsynaptic membrane area and the number of receptors in a synapse (Fig. 3c and Extended Data Fig. 6a), consistent with the idea that the function of these synapses could be altered independently either by changing the number of receptors or by modifying the organization of the postsynaptic protein network[32].

Intriguingly, the mean size of receptor networks in a synapse, when plotted against receptor concentration, was always larger than that for simulated randomly distributed receptors

(RDRs) or randomly distributed receptors without overlap (RDRs*) (Fig. 3d). Furthermore, the overall distribution of network size followed the power law (Fig. 3e and Extended Data Fig. 6b). The power law exponent (1.87), representing the fractural dimension of receptor networks, was smaller than that for RDR (2.44) and RDR* (2.40) (Fig. 3e). These results suggest that receptor networks tend to 'attract' more receptors to grow into larger networks, which is a property typically found in self-organizing processes near critical states[33].

To quantify the degree of orderliness for the receptor organization, we calculated Voronoi entropy that measures information content in the Voronoi tessellation of the receptor localizations[34] (Extended Data Fig. 6c). The Voronoi entropy becomes zero for a perfectly ordered structure, whereas, for a fully random 2D distribution of points, the value has been reported to be 1.71 (ref. [35]). The Voronoi entropy for our measured receptor distribution was 1.50, which was smaller than that for RDR (1.60) and RDR* (1.55) (Fig. 3f). The Voronoi entropy for the linked receptors was further reduced to 1.48 (Extended Data Fig. 6d). Thus, the smaller entropy for the measured receptors is likely to arise from the semi-ordered 2D networks. This Voronoi entropy value in between the entropy of crystal and liquid further suggests that the receptors organize in the mesophasic state. This mesophasic state is much more disordered than the liquid-crystalline state of acetylcholine receptors in the neuromuscular junction[36,37]. This could potentially allow for rapid change in receptor organization to serve as a plasticity mechanism in GABAergic synapses. Several synapses (12.9%) had Voronoi entropy larger than that of RDR (Fig. 3g). They are mostly synapses with fewer receptors that were unable to establish semi-ordered organization.

Mesophasic receptor assembly with a sharp phase boundary.

The semi-ordered receptor networks presumably reflect a mesophasic state of the self-organized PSD. If this is the case, one would expect that the mesophasic PSD might separate from the cytosol with a phase boundary. To test this, a smoothed convex hull of all linked receptors on the postsynaptic membrane (Fig. 4a and Extended Data Fig. 7a,b) was constructed. Within this hull that enclosed about 66% of the postsynaptic membrane area (Extended Data Fig. 7c), the receptor concentration was high (~3,000 μm^{-2}) and relatively uniform. This concentration dropped steeply within ~18 nm across the hull (Fig. 4b). Thus, the smoothed convex hull can, indeed, be considered as the phase-separating boundary of the mesophasic receptor assembly. Interestingly, the sharp boundary was characteristic only for the linked receptor, whereas the concentration of the solitary receptors changed only moderately across the convex hull (Fig. 4b). Thus, the solitary receptors appear to diffuse more readily into and out of the mesophasic assembly.

Alignment of receptor assemblies with condensates of scaffolding molecules.

It is known that $GABA_A Rs$ interact with scaffolding molecules that form thin, sheet-like densities in parallel to the postsynaptic membrane[7]. To examine whether such interactions might underlie the observed organization of $GABA_A Rs$, we obtained a 2D density projection of the scaffolding layer (Fig. 4a2). Distinct condensate-like densities were observed in the scaffolding layer (Fig. 4a2 and Extended Data Fig. 7b). For most (76%) synapses, the image density of the scaffolding layer inside the phase boundary was higher than that outside the phase boundary (Fig. 4c). Furthermore, many particles in the scaffolding layer positioned

directly underneath individual receptor densities, also with ~11-nm inter-particle distances (Fig. 4d). Quantitative analysis further confirmed that the density in the scaffolding layer was higher directly underneath a linked GABA$_A$R within the phase boundary (Fig. 4e). In contrast, the higher peri-receptor scaffolding density was not observed for receptors outside the phase boundary, nor was it found for solitary receptors within the phase boundary, indicating that such receptors might not have direct interactions with the scaffolding molecules (Fig. 4e). Thus, the semi-ordered organization of linked receptors is likely due to their interaction with the underlying scaffolding molecules, which form sheet-like condensates.

The high peri-receptor scaffolding densities of the linked receptors further provide a clue to resolve the interaction patterns between GABA$_A$Rs and scaffolding molecules. By 3D sub-tomogram classification, we observed four patterns of scaffolding molecules beneath receptor pairs (Fig. 4f). For about 58% of receptor pairs, densities in the scaffolding layers were better resolved (Fig. 4f1-3). Although their two-fold symmetric appearance could be biased by the receptor pairs, the presence of resolvable densities in the scaffolding layer beneath receptor pairs does indicate direct association between receptor pairs and scaffolding molecules. Furthermore, the three different patterns of resolvable scaffolding densities might suggest that such interactions could happen at different sites of scaffolding proteins, perhaps with different GABA$_A$R subunits. On the other hand, the density of scaffolding layer for about 42% of receptor pairs was smeared out (Fig. 4f4). This could be due to intrinsic flexibility of the intracellular domain of GABA$_A$R. Or, alternatively, these receptors did not anchor to the scaffolding proteins and formed 'pairs' by chance or by interactions with other molecules.

Monte Carlo simulation of the self-organization of GABA$_A$Rs with gephyrin molecules.

The predominant scaffolding molecule in GABAergic synapses is gephyrin, containing G and E domains that can form intermolecular trimer and dimer, respectively, leading to oligomerization of the gephyrin proteins[38,39]. The E domain of gephyrin also anchors intracellular loops of GABA$_A$Rs[40]. To test whether such multivalent interactions among gephyrin domains and GABA$_A$Rs can result in the mesophasic organization of GABA$_A$Rs, we performed Monte Carlo simulations taking those interactions into account (Extended Data Fig. 8 and Supplementary Table 3). GABA$_A$Rs and gephyrin molecules initialized with random distribution gradually clustered together in time (Fig. 4g and Supplementary Video 3). During this self-organizing process, the Voronoi entropy of the receptor organization reduced (Fig. 4h,i). Stronger receptor–gephyrin interactions (Fig. 4h) or gephyrin dimer and trimer interactions (Fig. 4i) resulted in less Voronoi entropy when the system reached a steady state. At the steady state, the simulated receptor organization recapitulated several key aspects of our experimental observations. First, the simulated receptor organization had a preferred NN distance, which correlated with the assumed length of gephyrin molecule (Fig. 4j). Second, the angle θ of the receptor triplets from the simulation was also relatively uniform between 60° and 180° (Fig. 4k). Third, a similarly sharp drop of receptor concentration was also observed at the convex hull of the simulated linked receptors, thus also defining a phase boundary (Fig. 4l). Therefore, the interactions among gephyrin

domains and receptors are sufficient to drive the self-organization of the mesophasic assembly of GABA$_A$Rs.

Mesophasic organization of PSD correlates with neurotransmitter release.

It is tempting to hypothesize that the mesophasic organization of GABA$_A$Rs might have functional significance with regard to synaptic function of neurotransmission. To test this, we analyzed the relative localizations of synaptic vesicles near the presynaptic membrane (Supplementary Table 2). In our tomograms, two types of such vesicles were identified: one tethered to the presynaptic membrane through rod-like densities, thus termed, hereafter, as tethered vesicles; the other had direct contact with the presynaptic membrane, thus termed, hereafter, as contacting vesicles (Fig. 4m). Both types of vesicle-plasma membrane interactions have also been observed in cryoET studies of purified synaptosomes[41]. Intriguingly, most (93%) of the contacting vesicles located within the presynaptic area apposing to the postsynaptic region inside the phase boundary (Fig. 4m and Extended Data Fig. 9) and the number of contacting vesicles outside the boundary were significantly fewer than expected from random distribution. In contrast, the number of tethered vesicles located inside or outside this area was not significantly different from the expected value based on random distribution (Fig. 4m and Extended Data Fig. 9). It has been suggested that tethering allows initial targeting of vesicles to the membrane, and the contacting vesicles are more ready to release upon stimulation[41,42]. If this is the case, our observations suggest that vesicular GABA is primarily released toward the semi-ordered GABA$_A$R networks within the mesophasic boundary, thus optimizing the efficiency of neurotransmission.

Discussion

In this study, we developed a template-free method to automatically identify molecular complexes in cryoET cellular tomograms. Analysis of such tomograms has traditionally been hampered by low signal-to-noise ratio and a highly crowded cellular environment. The method has enabled us to not only resolve the in situ structure of GABA$_A$R but also to determine the locations of individual receptors, their relative orientations and their interactions with scaffolding molecules at high accuracy without labeling. A potential caveat in GABA$_A$R identification is that GABAergic synapses might also contain glycine receptors (GlyRs)[43], a pentameric complex that is difficult to distinguish from GABA$_A$R. This is unlikely the case in our culture system where inhibitory postsynaptic currents were predominantly from GABA$_A$Rs rather than GlyRs (Extended Data Fig. 1a-e), and immunofluorescence staining for GlyRs revealed negligible puncta (Extended Data Fig. 1f-h). It is possible that some GlyRs existed in our system and were misidentified as GABA$_A$Rs; but, because of their small number, this might not affect the overall mesophasic organization of GABA$_A$Rs.

Recently, it was reported that GABA$_A$Rs and gephyrin molecules are organized into sub-synaptic nano-clusters by super-resolution optical imaging[18,21]. Both studies found about 30% of inhibitory synapses having two or more subsynaptic 'nanodomains' and 70% having only one uniformly organized synaptic 'domain' of receptor molecules. In our observations, the overwhelming majority of synapses should be classified as 'uni-domain' synapses. Even

though many of these synapses each contained multiple separate 2D GABA$_A$R networks, those networks apparently formed a single assembly (Fig. 3b and Extended Data Fig. 7b). In a few cases (3 of 72), we did observe two discretely separated receptor assemblies within one synapse. Among these, two synapses each had a narrow band within the synaptic cleft that separated the two receptor assemblies (Extended Data Fig. 10a,b). The third had a bent and deformed membrane that caused the separation of the assemblies (Extended Data Fig. 10c). Thus, at least in our culture system, GABA$_A$Rs on inhibitory postsynaptic membranes form a uni-domain organization, except for rare cases where physical barriers restricted receptors and scaffolding molecules.

The inhibitory PSD was proposed to form a hexagonal lattice organization based on the trimer and dimer interaction among gephyrin domains observed in biochemical studies. This classical model implicitly assumes rigid interactions among the molecules[44]. However, gephyrin and receptor molecules are intrinsically flexible owing to the disordered linker domains of gephyrin molecules, the disordered intracellular domains of GABA$_A$Rs and the weak multivalent interactions among the proteins. Indeed, gephyrin molecules have been found to form irregular meshes rather than hexagonal lattice in vitro under EM[38]. Our observation of the 2D network of GABA$_A$Rs with a uniform relative angle θ and our simulation that recapitulated a rather semi-ordered organization suggest that gephyrin molecules also form similar networks to drive the mesophasic assembly of GABA$_A$Rs. Besides gephyrin, the mesophasic organization of this receptor–scaffolding system might also involve other proteins, such as GARLH4 and Shisa7, both of which are known to regulate GABA$_A$R localization and inhibitory synaptic transmission[27,28].

In conclusion, our results reveal a hierarchical organization of GABA$_A$Rs, from receptor super complex to receptor network to mesophasic assembly, that is functionally correlated to the presynaptic neurotransmitter release. This mesophasic assembly exhibits both variability and regularity, demonstrating how ensembles of synaptic molecules acquire great complexity via self-organization. This organization principle might also suggest a molecular strategy for a synapse to achieve its 'Goldilocks' state, with a delicate balance between stability and flexibility on the micro-nano scale.

Online content

Any methods, additional references, Nature Research reporting summaries, source data, extended data, supplementary information, acknowledgements, peer review information; details of author contributions and competing interests; and statements of data and code availability are available at https://doi.org/10.1038/s41593-020-00729-w.

Methods

Primary culture of hippocampal neurons.

All animal experiments were approved by the Animal Experiments Committee at the University of Science and Technology of China (approval nos. USTCACUC1201026 and USTCACUC403014). Low-density cultures of dissociated embryonic rat hippocampal neurons were prepared according to the protocols described previously[7]. In brief, EM gold

finder grids (Quantifoil R2/2 Au NH2 grids) and coverslips were plasma cleaned with H_2 and O_2 for 10 s using a plasma cleaning system (Gatan), sterilized with ultraviolet light for 30 min and then treated with poly-L-lysine before use. Hippocampi of randomly selected embryonic day-18 embryos (without distinguishing sex difference) from timed-pregnant Sprague–Dawley rats (CD(SD) IGS, Beijing Vital River Laboratory Animal Technology) were dissected. The hippocampi were treated with trypsin for 15 min at 37 °C. The dissociated cells were plated on the treated EM grids or coverslips at a density of 40,000–60,000 cells per ml in 35-mm Petri dishes and maintained in incubators at 37 °C in a 5% CO_2 atmosphere. NeuroBasal medium (Invitrogen) supplemented with 5% heat-inactivated bovine calf serum (PAA), 5% heat-inactivated fetal bovine serum (HyClone), 1× GlutaMAX (Invitrogen) and 1× B27 (Invitrogen) was used as culture medium. To each Petri dish, 1.5 ml of medium was added. Twenty-four hours after plating, half of the medium was replaced with serum-free culture medium. Then, one-third of the culture medium was replaced with fresh serum-free culture medium every 3 d. The cultures were treated with cytosine arabinoside (Sigma-Aldrich) to prevent the overgrowth of glial cells. Some of the cultures experienced inactivation by 2-d treatment with 1 μM tetrodotoxin (TTX) or 1-h treatment with 2 μM TTX followed by 3-h treatment with 2 μM TTX plus 50 μM APV[45,46]. We did not observe significant differences among different groups in basic properties of receptor expression and organization and, thus, pooled the data together for all analyses. For cryo-correlative light microscopy (LM) and EM (cryoCLEM) experiments, cultures were infected with lentivirus containing a vector encoding mCherry-gephyrin fusion protein at 10 d in vitro (DIV), as described previously[7]. The plasmid *mCherry-gephyrin* was a gift from A. M. Craig at the University of British Columbia.

Electrophysiology.

Whole-cell perforated patch-clamp recordings were used to measure inhibitory postsynaptic currents (IPSCs) from cultured neurons at 14–18 DIV. Glass electrode (Kimble Chase, pulled to 2.5–3 MΩ) were tip-filled with internal solution and then filled with amphotericin B (200 μg ml^{-1}, Sigma-Aldrich) containing internal solution, containing (in mM) 136.5 K-gluconate, 9 NaCl, 0.2 EGTA, 10 HEPES and 1 $MgCl_2$ with pH adjusted to 7.3 by NaOH. External bath solution (for example, extracellular solution (ECS)) contained (in mM) 150 NaCl, 5 glucose, 10 HEPES, 3 KCl, 2 $MgCl_2$ and 3 $CaCl_2$, pH 7.3. IPSCs were recorded in the presence of 10 μM 6-cyano-7-nitroquinoxaline-2,3-dione (CNQX; Tocris). 1 μM strychnine (Sigma-Aldrich) or 20 μM bicuculline methiodide (BMI; Tocris) was used to block glycine receptors or $GABA_A$ receptors, respectively. Recordings were performed using MultiClamp 700B amplifiers (Molecular Devices) and custom IGOR-based programs. To evoke synaptic or autaptic IPSCs, neurons were voltage clamped at −70 mV, and brief stimulations (100 mV, 1 ms) were given every 20 s. Only neurons showing constant input resistance (100–350 MΩ) throughout the experiment and stable evoked IPSCs during the control period were accepted for analysis. For spontaneous IPSC analysis, neurons with fewer than 50 events were excluded.

Immunostaining and confocal fluorescence imaging.

Cultured neurons on coverslips at 16 DIV were incubated in ECS solution containing 1 μg ml^{-1} (1:1,000 dilution) of polyclonal rabbit antibody against $GABA_A$R γ2 subunit (cat. no.

224003, Synaptic Systems) and 2 μg ml^{-1} (1:500 dilution) of monoclonal mouse antibody against GlyR α1 subunit (cat. no. 146011, Synaptic Systems) at 37 °C for 15 min. After that, the cells were fixed in PBS containing 3% paraformaldehyde for 20 min and then treated with 0.2% Triton-X100 in PBS for 6 min. The neurons were then blocked with 3% BSA in PBS for 1 h and then incubated in diluted secondary antibody solution (for example, PBS containing 3% BSA, 1.5 μg ml^{-1} (1:1,000 dilution) of Alexa 488-labeled anti-mouse antibodies (cat. no. 715–546-150, Jackson ImmunoResearch) and 1.5 μg ml^{-1} (1:1,000 dilution) of Alexa 647-labeled anti-rabbit antibodies (cat. no. 711-606-152, Jackson ImmunoResearch)) at room temperature for 40 min.

Fluorescence images of GABA$_A$Rs and GlyRs were obtained using a Zeiss LSM 710 confocal microscope with a ×63 oil immersion objective. Dual-channel fluorescence images were collected using illumination light at 488-nm and 633-nm wavelengths for GlyR and GABA$_A$R imaging, respectively.

Frozen-hydrated sample preparation.

At DIV 16, the culture medium was replaced with ECS immediately after the cultures were taken out of the CO$_2$ incubator. The grids were loaded into a plunge freezer (Vitrobot IV, Thermo Fisher), which was maintained in 100% humidity. Protein A-coated colloidal gold beads (15-nm size, CMC) were added to the grids (4 μl each; stock solution was washed in ECS and diluted ten times after centrifugation) as fiducial markers. The grids were then blotted and plunged into liquid ethane and stored in liquid nitrogen until use.

CryoCLEM imaging.

For cryoCLEM imaging, we used the same procedures as detailed in our previous paper[7,47]. In brief, the inside channel of the custom-built cryo-chamber was pre-cooled to −190 °C by liquid nitrogen and maintained below −180 °C. Then, an EM grid with frozen-hydrated sample was loaded onto an EM cryo-holder (Gatan), which was subsequently inserted into the cryo-chamber. Dry nitrogen gas flowed around the ×40 objective lens (Olympus LUCPLFLN 40X, NA 0.6) throughout the experiment to prevent the formation of frost. Fluorescence images were taken with an Andor Neo sCMOS camera (Andor) attached to the fluorescence microscope. For each field of view, both bright-field and mCherry channel (Ex: 562/40, DM: 593, Em: 641/75; Semrock, mCherry-B-000) images were acquired.

The EM cryo-holder with the grid was then directly transferred into a Tecnai F20 microscope (Thermo Fisher). Indexes of the finder grids were used to roughly identify the areas of the sample imaged in cryo-light microscope. Then, the Midas program in the IMOD package[48] was used to roughly align the low-magnification (×330) EM images with the bright-field LM images. After rough alignment, a set of holes (about ten for each image) on the carbon film of the grid were manually picked using 3dmod in the IMOD package from both the low-magnification EM images and their corresponding fluorescence images. Transformation functions between the EM and LM images were calculated by correlating the selected positions in both images.

After aligning the low-magnification EM images with LM images, pixel-wise positions of ~15 holes on carbon film (in one square) in each low-magnification EM image were

recorded. Afterwards, those holes were identified at ×5,000 magnification, and their mechanical coordinates (that is, positions on the EM sample stage) were also recorded. The transformation function from the pixel-wise positions to EM mechanical coordinates was determined. Then, the puncta of gephyrin-mCherry were selected manually using 3dmod in IMOD. Positions of these fluorescent puncta were then converted into corresponding EM mechanical coordinates with the transformation functions to guide tilt series acquisition. Finally, reconstructed tomographic slices were aligned and merged with the fluorescence images to identify each synapse (Fig. 1a) using Midas and ImageJ.

CryoET imaging.

For cryoCLEM experiments, the tilt series were collected using a Tecnai F20 microscope equipped with an Eagle CCD camera (Thermo Fisher). The Tecnai F20 was operated at an acceleration voltage of 200 kV. Tilt series were collected first from 0° to −60° and then from +2° to +60° at 2° intervals using FEI Xplore3D software, with the defocus value set at −12 to −18 μm and the total electron dosage of about 100 e$^-$/Å^2. The final pixel size was 0.755 nm.

For the analysis of GABA$_A$Rs, cryoET data were collected using a Titan Krios (Thermo Fisher) equipped with a Volta phase plate (VPP), a post-column energy filter (Gatan image filter) and a K2 Summit direct electron detector (Gatan). The energy filter slit was set at 20 eV. The Titan Krios was operated at an acceleration voltage of 300 KV. When VPP was used, the defocus value was maintained at −1 μm; otherwise, it was maintained at −4 μm. The VPP was conditioned by pre-irradiation for 60 s to achieve an initial phase shift of about 0.3π. Images were collected by the K2 camera in counting mode or super-resolution mode. When counting mode was used, the pixel size was 0.435 nm. For super-resolution mode images, the final pixel size was 0.265 nm. Tilt series were acquired using SerialEM[49] with two tilt schemes: 1) from +48° to −60° and from +50° to +66° at an interval of 2° and 2) from +48° to −60° and from +51° to +66° at an interval of 3°. The total accumulated dose was ~150 e$^-$/Å^2. For sub-tomogram analysis, six grids were used for data collection. In total, 32 and 40 inhibitory synapses were imaged with and without VPP, respectively.

3D reconstruction of the tomograms.

Each recorded movie stack was drift corrected and averaged to produce a corresponding micrograph using MotionCorr[50]. To combine the data with different pixel sizes during image processing, we rescaled the images recorded with super-resolution mode with an antialiasing filter to match the pixel size of images recorded with counting mode (0.435 nm per pixel) by *newstack* command in IMOD. For images recorded without VPP, the defocus value of each image was determined by CTFFIND4 (ref. [51]). For tilt series acquired with VPP, the defocus values cannot be precisely calculated. However, the defocus of each image is relatively low (~1 um), which does not limit the resolution obtained by sub-tomogram averaging. Thus, we did not perform defocus determination and contrast transfer function (CTF) correction for these tilt series.

Tilt series were aligned with 15-nm gold beads as fiducial markers using IMOD. 3D reconstruction was performed with the weighted back-projection (WBP) algorithm using

NovaCTF[52]. Because those tomograms had low contrast and were difficult to interpret by visual inspection, we also used the SIRT-like filter in NovaCTF to generate tomograms equivalent to those reconstructed by the SIRT algorithm with five iterations. Segmentation and cryoET density analyses were performed using the SIRT-like filter reconstructed tomogram, whereas sub-tomogram averaging was performed using tomogram reconstructed with WBP.

Because the samples are thick, to eliminate the depth-of-the-focus problem, we performed 3D-CTF correction[52] and obtained CTF phase-flipped tomograms for tilt series acquired without VPP. The defocus step for depth-of-the-focus correction was 50 nm.

3D rendering.

By manually placing markers corresponding to structures using *volume tracer* in UCSF Chimera[53], synaptic membranes and organelles, such as microtubules, actin filaments, mitochondria and multivesicular bodies, were traced and segmented. Then, the manually segmented structures were smoothed by Gaussian filter. The ribosomes and synaptic vesicles were identified by template matching using PyTom[54], as described previously[7]. The vesicles were rendered based on their sizes.

Generating uniform oversampled points on postsynaptic membranes.

Previous studies showed that sub-tomogram averaging can be performed with uniform selected sub-tomograms on a given surface, taking advantage of the geometry of that surface[55,56]. We thus sought to reconstruct the structure of $GABA_AR$ by uniform oversampled sub-tomogram on the postsynaptic membrane segmented manually. Postsynaptic membrane was defined as the synaptic membrane area corresponding to the uniform synaptic cleft.

To segment postsynaptic membrane, we first segmented the synaptic cleft volumes in two-times binned tomograms using a segmentation tool in Amira (Thermo Fisher). As the pixel size of all tomograms was or was scaled to 0.435 nm per pixel, the pixel size of two-times binned tomograms was 0.87 nm per pixel. Then, we used the Sobel filter to generate boundary surface of the segmented synaptic cleft. This boundary represented two opposed membranes: presynaptic and postsynaptic. Then, the postsynaptic membrane was manually extracted.

To generate uniformly oversampled points, we first generated a uniformly distributed 3D lattice of hexagonal close-packaging points in two-times binned tomograms (Extended Data Fig. 2a). The distance between the two nearest sampling points in the lattice was five pixels (4.35 nm). All the sampling points were within 8.7-nm distance to the segmented membrane. The two-times binned sub-tomograms, whose centers are the sampling points, were then extracted using the *boxstartend* program in IMOD. The extracted box size of each sub-tomogram was $32 \times 32 \times 32$ pixels ($27.84 \times 27.84 \times 27.84$ nm). Because the sampling distance was five pixels, the nearest distance from the center of any possible receptor to the one sampling point was less than 2.5 pixels. Given the 7-nm (~8-pixel) diameter of $GABA_AR$, each receptor should be fully covered in multiple extracted sub-tomograms so that no receptor was omitted during sampling.

The orientation of each sub-tomograms has three Euler angles denoted as parameters within the Relion star file[25]: rot (_rlnAngleRot), tilt (_rlnAngleTilt) and psi (_rlnAnglePsi). During the sub-tomogram extraction, the initial tilt and psi angles of each sub-tomogram were calculated as the orientation perpendicular to the patch of membrane in that sub-tomogram. The rot angle (rotational angle around the vector that is perpendicular to the membrane) for each sub-tomogram was set randomly.

With the uniform oversampling, we obtained 171,374 and 135,717 two-times binned sub-tomograms near the postsynaptic membrane from tomograms imaged with and without VPP, respectively.

Initial 3D classification using two-times binned sub-tomograms.

The classification and refinement of the sub-tomograms were performed using Relion (Extended Data Fig. 2b)[25,57]. The tomograms imaged with and without VPP appeared to be with different contrast. It is possible that 3D classification classifies the same protein feature into different classes based on whether or not the sub-tomogram was acquired with VPP. To minimize this error of classification, we performed the classification separately for sub-tomograms imaged with VPP and without VPP. This separation also enables cross-validation between results obtained from data acquired with VPP and without VPP (Extended Data Fig. 2b).

To identify GABA$_A$Rs from those sub-tomograms, we performed 3D classification imposing five-fold symmetry using Relion3. The resolution for the classifications was limited to 30 Å. To ensure that the orientation was searched around the vector perpendicular to membrane, we set the prior of tilt and psi angles as the calculated angles corresponding to the orientation of membrane and set the sigma of local angle search for tilt and psi angles as 3°. We did not set any limitations in searching for the rot angle during classification. To limit the 3D positional search during 3D classification, the prior of the offset searching range was set as zero, meaning that the offset was searched only around the center of the sub-tomograms. The offset search range was set to ±3 pixels. The initial reference was generated by *relion_reconstruct* using the predetermined Euler angles. As expected, the initial reference appeared as a flat membrane structure due to the averaging of uniform oversampled sub-tomograms on the membrane (Extended Data Fig. 2c). Because tilt series imaged without VPP were corrected using 3D-CTF, and the tilt series imaged with VPP were recorded at low defocus value (−1 μm), we did not perform CTF correction during image processing using Relion. To compensate for missing wedge, missing wedge volumes (_rlnCTFimage in relion star file), which were 3D masks in Fourier space, were generated by custom scripts. The classifications were performed with 100 iterations (Extended Data Fig. 2c).

To determine the optimal number of classes for 3D classification, we tested the number of classes from 8 to 15 in classification. We obtained one 'good' class, which appeared similarly to previously published GABA$_A$R structures, for all number of classes from 8 to 13 during the classification. The number of sub-tomograms in the 'good' class reduced as the number of classes increased from 8 to 11 but became stable after 11 (Extended Data Fig. 3a). The structures of the classification result became worse when the number of classes was

larger than 13. Thus, we used 12 as the optimal number of classes for classification and obtained the 'good' class among the 12 classes for both of the classifications using data collected with and without VPP (Extended Data Fig. 2b).

To eliminate that two or more sub-tomograms corresponding to the same receptor, we removed duplicated sub-tomograms as follows. We mapped the refined positions of the sub-tomograms after 3D classification to the original tomograms. If distances between the centers of two classified sub-tomograms in original tomograms were smaller than 7 nm (the diameter of GABA$_A$R), the sub-tomogram with the lower score (_rlnLogLikelihoodContribution in Relion star file) was removed. After removing duplicates, we obtained 7,089 and 5,004 sub-tomograms from data acquired with and without VPP, respectively.

First round of 3D refinement using unbinned sub-tomograms.

Next, we calculated the coordinates of sub-tomograms in the corresponding unbinned original tomograms (with the pixel size of 4.35 Å per pixel) and extracted new sub-tomograms with a box size of $64 \times 64 \times 64$ pixels. We combined sub-tomograms from VPP and no-VPP data for 3D auto-refine (Extended Data Fig. 2b). Then, we generated 60-Å resolution initial references by *relion_resonstruct* with the predetermined orientations. Differing from the previous round of classification, we did not limit the search angle and did not set prior for angle and offset searching during the 3D refinement. Five-fold symmetry was imposed during 3D refinement. This round of 3D auto-refinement refined the orientation and the positions of sub-tomograms and generated a preliminary reconstruction at 21-Å resolution, which was reported during *relion_refine* processing. The duplicated sub-tomograms were further removed. After this step, we obtained 6,919 and 4,904 sub-tomograms for VPP and no-VPP data, respectively.

Removing outliers of tilt and psi angles.

Because synaptic membrane is relatively flat, and GABA$_A$Rs are perpendicular to the membrane, the tilt and psi angles for sub-tomograms should be similar in a given synapse. Thus, we used this knowledge to further reduce the error of receptor identification, as follows. We plotted the distributions of tilt and psi angles for the sub-tomograms in each synapse (Extended Data Fig. 3b,c). Indeed, the distribution of the refined tilt and psi angles of sub-tomograms in a given synapse was in a cluster with approximately Gaussian distribution, whose center corresponded to the angles perpendicular to the postsynaptic membrane (Extended Data Fig. 3c). Few sub-tomograms have orientations perpendicular to the membrane but, pointing to the cytoplasmic side, possibly they were aligned to the proteins of PSDs on the cytoplasmic side. We discarded those sub-tomograms for further refinement. The percentages of those misaligned sub-tomograms with opposite orientation were 2% and 5% for VPP and no-VPP data, respectively (Extended Data Fig. 3d). Furthermore, we also excluded sub-tomograms whose tilt and psi angles were three times of s.d. (σ) away from the center of the Gaussian distribution (10% and 13% of total sub-tomograms from VPP and no-VPP data, respectively) (Extended Data Fig. 3c-e).

Removing outliers of low score.

Next, we removed sub-tomograms with lower scores (_rlnLogLikelihoodContribution in Relion star file). We normalized the scores of sub-tomograms in each synapse, ensuring that the normalized scores of the sub-tomograms for each synapse had an average of 0 and an s.d. of 1. The distribution of normalized scores was a slightly lopsided Gaussian distribution (Extended Data Fig. 3f). We fitted the distribution with a Gaussian distribution and then removed the sub-tomograms with scores lower than mean minus 2σ. The ratio of sub-tomograms with a lower score was ~3% for both VPP and no-VPP data (Extended Data Fig. 3e-g).

Second round of 3D refinement using unbinned sub-tomograms.

After removing outliers, those sub-tomograms were used for the second round of 3D auto-refinement (Extended Data Fig. 2b). Local searches with a sigma angle of 3° for orientation determination were performed during 3D auto-refinement. Five-fold symmetry was imposed during 3D refinement. The final resolution of the reconstruction was estimated with two independently refined maps from halves of the data set with gold standard Fourier shell correlation at the 0.143 criterion[58] using *relion_postprocess* and was determined to be 19 Å (Fig. 1g).

Analysis of the accuracy of rot angle.

To estimate the accuracy of rot angle, we calculated two sets of cross-correlation (CC) scores for the original sub-tomograms and sub-tomograms that rotated 36° (Extended Data Fig. 3h). CC score represents the similarity between a sub-tomogram and the sub-tomogram average of $GABA_AR$. To do so, we rotated the sub-tomogram average by 36° and then processed the sub-tomograms with *relion_refine* using original and rotated sub-tomogram averages as references, separately. We skipped both the maximization step and the alignment step to prevent updating references and orientation search, respectively. We used *always_cc* argument to calculate the CC score instead of log-likelihood, which was the default in Relion. The processes were finalized with one interaction. By this processing, we obtained two new star files with the CC scores. We plotted the distribution of CC scores in the two star files. Indeed, the score distributions for the two sets of sub-tomograms were well separated (Extended Data Fig. 3h, i).

Estimating the error rate of receptor identification.

To estimate the error of our 3D classification with uniformly oversampled sub-tomograms, we visually inspected all the identified receptors in four selected tomograms acquired with VPP. A few receptors identified by our methods cannot be recognized; thus, those receptors could be falsely identified. Thus, the error rate was defined as the percentage of identified receptors that cannot be recognized visually for each synapse.

The error rates for the four synapses were 14.4% (16 of 111), 6.0% (5 of 83), 22.9% (32 of 140) and 18.3% (62 of 339), respectively.

False-positive rate of receptor identification.

To evaluate the false-positive rate of GABA$_A$R identification, we repeated the sub-tomogram analysis using data mixing the same sub-tomograms and intentionally induced negative-controlled sub-tomograms on the presynaptic membrane (Extended Data Fig. 4). These negative-controlled sub-tomograms were extracted using the same uniform oversampling methods on the segmented presynaptic membranes. Presynaptic membranes of two inhibitory synapses imaged with VPP and two inhibitory synapses imaged without VPP were used for this analysis.

We did the classifications and refinements (Extended Data Fig. 4a,b) exactly the same as the previously described steps. The classifications and refinements with data mixing with negative-controlled sub-tomograms also generated structures of GABA$_A$Rs. As expected, the number of GABA$_A$Rs identified using sub-tomograms with negative-controlled sub-tomograms for each synapse was similar to the receptor identified without negative-controlled sub-tomograms (Extended Data Fig. 4c).

For synapses analyzed for both presynaptic and postsynaptic membranes, we calculated the false-positive rate as falsely identified receptors on presynaptic membranes divided by the number of receptors on postsynaptic membranes. The false-positive rates for the two synapses imaged with VPP were 15% and 10%; the false-positive rates for the two synapses imaged without VPP were 13% and 10% (Extended Data Fig. 4d).

3D classification of the oversampled sub-tomograms without symmetry.

We also tested whether the classification without symmetry could yield structures similar to the GABA$_A$R structure published before. We used the same sub-tomograms acquired with VPP and performed the classification without symmetry. The other parameters were the same as the first-round classification described before. Indeed, this classification generated structures with sizes similar to the GABA$_A$R. However, the structures were worse than the reconstruction with five-fold symmetry and were not centered properly (Extended Data Fig. 5d). Intriguingly, two receptor-like structures could present in the same sub-tomogram average (Extended Data Fig. 5e). This further confirmed that the receptors tend to form receptor pairs with 11-nm IRD.

Analysis and reconstruction of receptor pair.

For each receptor pair (with 11 ± 4-nm inter-particles distance), we calculated the coordinate of the center of the two GABA$_A$Rs and used this coordinate to extract sub-tomograms ($64 \times 64 \times 64$ pixels) in two-times binned original tomograms. The tilt and psi angles of a receptor pair were set as the mean of those angles for the two receptors. The rot angle was calculated to ensure that the vector from one receptor to the other receptor aligned to the x axis of the receptor pair reconstruction (Fig. 2f). We then reconstructed the receptor pair using *relion_reconstruct* with the calculated orientations. In total, 16,234 sub-tomograms of receptor pairs were used in the reconstruction.

Measuring the angle (ω) between the rotation of the receptor and pair axis.

We then calculated the angle (ω) between the rot angle of one given receptor in a receptor pair to the receptor pair axis (Fig. 2g). The receptor pair axis was defined as a vector from the other receptor to the given receptor. Then, we separated the sub-tomograms into four groups by the ω angle: 0–18°, 18–36°, 36–54° and 54–72° groups, containing 3,883, 3,957, 4,199 and 4,195 sub-tomograms, respectively. We further reconstructed the sub-tomograms in each group using *relion_reconstruct*. In all four reconstructions, the given receptor appeared to have pseudo five-fold symmetry.

Reconstructing receptor triplet and analyzing the angle θ between the two arms.

One GABA$_A$R can also pair with two neighboring receptors forming a receptor triplet. Each triplet has two arms, which connect the central receptor to the two neighboring receptors. We then calculated the angle θ between the two arms of the triplet (Fig. 2i). We reconstructed the triplets with 50–70°, 80–100°, 110–130° and 160–180° of θ value, containing 2,428, 1,772, 1,937 and 1,714 sub-tomograms, respectively (Fig. 2j). The center of each receptor triplet sub-tomogram was set as the mass center of the three receptors. Tilt and psi angles of each sub-tomogram were set as the mean angles of the three receptors. The rot angle of a receptor triplet sub-tomogram was calculated to ensure that the vector from one neighboring receptor to the other was parallel to the *x* axis. All reconstructions were computed using *relion_reconstruct* by the sub-tomograms (64 × 64 × 64 pixels) extracted from two-times binned tomograms.

3D classification of densities of scaffolding layer underneath receptor pair.

To test whether scaffolding densities contribute to the receptor pair formation, we did focused classification of the scaffolding region of the receptor pairs. We first chose the receptor pair sub-tomograms with 11 ± 2-nm inter-particle distance. A cuboid mask with 13.92 nm in length along the *x* direction, 8.7 nm in width along the *y* direction and 8.7 nm in height along the *z* direction was applied on the scaffolding layer to pre-form 3D focused classification. The classification was done with two-fold symmetry and without orientation or position search. From a total of 10,222 sub-tomograms, four classes were generated, containing 1,786, 1,330, 2,794 and 4,312 sub-tomograms, respectively (Fig. 4f).

Local receptor concentration and NN distance analysis.

Among the 72 synapses that we obtained, two of them imaged without VPP were not fully covered in the tomograms. These two synapses were excluded in the analyses of GABA$_A$R distribution in the following sections.

We calculated the concentration of receptors around a given point on the membrane. In our case, the given point was either a receptor or a randomly selected point on the postsynaptic membrane. We partitioned the membrane around the given point into concentric rings of 2-nm width. The radius range of the rings was from 0 to 32 nm. Then, the receptor concentration was calculated as the number of receptors in a ring divided by the surface area of that ring.

We also calculated the first and second NN distance for each receptor, using the standard distance formula in 3D.

Analysis of the receptor networks.

If two receptors had a distance smaller than 15 nm, they were defined as 'linked' receptors. We then defined a receptor network as follows. If two receptors were linked by a series of (equal to or more than zero) receptors, we grouped them in the same network. Otherwise, they were in different networks. The network size was defined as the number of receptors in a network. Randomized receptor distributions were generated from the same number of receptors over the same postsynaptic area.

Calculation of the Voronoi entropy.

To calculate the Voronoi entropy of each synapse, we first calculated the first two singular vectors for all 3D segmented points on postsynaptic membrane, using singular value decomposition in MATLAB. Using the two singular vectors, we projected the 3D receptor locations on a 2D plane. Then, we generated Voronoi tessellation of the 2D locations of receptors in each synapse (Extended Data Fig. 6c) using the scipy.spatial.Voronoi function in SciPy (https://scipy.org). Voronoi entropy was calculated using the following formula[34]:

$$V = -\sum_i p_i ln(p_i)$$

where i is the number of vertices of a polygon, p_i is the frequency of the polygon with i vertices, ln is the natural logarithm and V is the Voronoi entropy.

Determining the boundary of mesophasic assembly of GABA$_A$Rs.

To determine the boundary of the receptor assembly, the receptor positions were first projected onto the 2D plane as described before. Then, a convex hull of all linked receptors for each synapse was constructed using the Python package *shapely* (https://github.com/Toblerity/Shapely). To eliminate the coincidently formed linked receptors outside the region of the condensed receptor, we smoothed the convex hull by 40-nm erosion followed by 40-nm dilation using the Python package *shapely* (Extended Data Fig. 7a). Convex hulls of 12 (out of 70) synapses had a diameter smaller than 80 nm. Those synapses were not eligible for dilation, so they were excluded in the phase boundary analysis. The distance of a receptor to the mesophase boundary was also calculated using *shapely*.

Calculation of synaptic membrane area.

To calculate the area of postsynaptic membrane, we first generated the surface of the postsynaptic membrane in 3D using *imodmesh* in IMOD. The area of postsynaptic membrane was extracted from the output of the *imodinfo* command in IMOD. Whereas in Fig. 4b and Extended Data Fig. 7c, the postsynaptic membranes were projected to a 2D plane. Thus, in those figures, membrane areas were calculated two dimensionally using *shapely*.

Analyzing image density of the scaffolding layer.

To analysis the image density of the scaffolding layer, we first extracted the voxels in the scaffolding layer region in the tomogram as densities 10–15 nm toward the cytoplasmic side from the postsynaptic membrane. The scaffolding layer region was then projected to a 2D plane, using two singular vectors of postsynaptic membrane described previously, resulting in 2D density profiles of the scaffolding layer parallel to the postsynaptic membrane. The mesophase boundary of GABA$_A$Rs was mapped on the 2D profile of the scaffolding layer. Densities inside and outside the mesophase boundary on the 2D profiles were calculated as the mean pixel density inside and outside of the boundary, respectively (Fig. 4c).

We then calculated the density of the scaffolding layer around 2D projected locations of receptors (Fig. 4e). To do so, the 2D density profiles were normalized so that the mean pixel density of the profiles was 0 and the s.d. was 1. We then partitioned the 2D profile of the scaffolding layer around a receptor into concentric rings of 5-nm width. The radius range of the rings was from 0 to 50 nm. The densities of the scaffolding layer were calculated as the mean intensity value both in the concentric ring and inside the postsynaptic membrane area (Fig. 4a). Hence, we produced the relation between the distance to the given receptor and the pixel density values of the 2D profile of the scaffolding layer.

Monto Carlo simulation of receptor and gephyrin organization.

N (N = 500) gephyrin molecules and Nr (Nr = 100) receptors were initialized with random distribution in an L × L (L = 500 nm) 2D plane in our simulation. A gephyrin molecule was simplified as two points, representing G domain and E domain, with a linker in between the two domains (Extended Data Fig. 8). The sizes of the G domain and E domain were 3 nm and 5 nm, respectively. Receptors were simplified as particles in our simulation. Both gephyrin and receptor molecules did random walk in the 2D plane with diffusion coefficient D (D = 10 nm^2 s^{-1}). For simplicity, we ignored the size of the receptor, so that two neighboring receptors could clash with each other.

Three types of gephyrin–gephyrin interactions were simulated as follows:

The first type of interaction was direct trimerization of gephyrin G domains (Extended Data Fig. 8a). When the distances among three gephyrin G domains are less than 4.5 nm, they bind with each other and form a trimer. The linker and the E domains together can rotate around the center. The angle between the two linkers can vary from 60° to 300°.

The second type is trimerization of gephyrin G domains through a dimer intermediate of gephyrin G domains (Extended Data Fig. 8b). With the probability Kc = 0.001, two gephyrin G domains can join with each other when their distance is less than 4.5 nm, with the linker and the E domains rotating together around this joint from 60° to 300°.

The third type is dimerization of gephyrin E domains (Extended Data Fig. 8c). If the distance between two gephyrins' E domains is less than 5 nm, the two domains bind together forming a dimer. The linker with G domains can rotate around the joint of two E domains from 162° to 198°.

With the three types of interactions, gephyrin molecules can interact with each other to form clusters. Reversely, dimers and trimers can dissociate with the probability K_t and K_d, respectively. In our simulations, K_d and the K_t were set to the same value (Supplementary Table 3).

The intracellular loops of receptors can bind to the dimers of gephyrin E domains. Although both interaction sites in the E domain dimer can bind to one receptor each, due to the steric effect, one dimer can bind to only one receptor. In our simulation, a receptor could bind to one dimer of gephyrin E domains when they were within 3.0 nm. Receptors can also dissociate from the dimers of gephyrin E domains with the probability K_r.

All the simulations were performed with 100,000 steps of random walk. The simulations (shown in Supplementary Table 3) were repeated 28 times for each set of parameters. The calculation of Voronoi entropy, NN distance, relative angle (θ) and phase boundary were performed with the methods described above.

Analysis of tethered and contacting synaptic vesicles.

To calculate the distance from synaptic vesicle to mesophase boundary, we first manually selected positions on the presynaptic membrane nearest to a contacting or a tethered vesicle. Then, the positions were projected to the 2D plane of the receptor positions using the methods described before. The distance (*d1*) from the synaptic vesicle projection point to the mesophase boundary was calculated using *shapely*. The value of *d1* was negative when the point was outside the mesophase boundary. We also projected all segmented points on the postsynaptic membrane inside the mesophase to the 2D plane and calculated the largest distance (*d2*) from those points to the mesophase boundary. The normalized distance from synaptic vesicle to mesophase boundary was calculated as *d1/d2*. Randomized vesicles were generated by randomly selecting locations over the same synaptic area. We repeated the randomization ten times for each synapse. The mean numbers of randomized vesicles inside or outside of the mesophase boundary were used for statistical analysis.

Statistics and reproducibility.

Sample size. No statistical methods were used to predetermine sample size. The sample size was determined by the 2 months of EM time available for us to perform cryoET imaging. After processing, we discovered that those data have high quality sufficient for obtaining 19-Å resolution reconstruction of $GABA_AR$ and for visualizing the distribution of receptors on each synapse.

Data exclusion.

Among the 72 synapses we obtained, two were not fully covered in the tomograms. These two synapses were excluded in the analyses of $GABA_AR$ distribution because, although the two synapses did contain $GABA_ARs$, they were not intact, and the distribution of $GABA_ARs$, such as the number of receptors for each synapse, cannot be estimated at all. For the phase boundary analysis, we excluded 12 (of 70) synapses that had a diameter smaller than 80 nm. Because we used a 40-nm erosion followed by a 40-nm dilation algorithm to determine the mesophase boundary, this algorithm cannot calculate the phase boundary of

those small synapses. These data exclusion criteria were not previously established but were derived from the limitations of the acquisition or processing procedures.

Replication and validation.

For each related figure, how many times each experiment was repeated independently with similar results is listed in the figure legends. We further used two strategies to reproduce our classification and refinement of $GABA_AR$ structures. First, the original tomograms were separated into two groups: acquired with or without phase plate. Using data from either group, similar structures of $GABA_AR$ could be obtained, indicating that the sub-tomogram averaging can be reproduced by half of the data. Second, we performed another independent processing of all the tomograms but added randomly picked sub-tomograms from the presynaptic membranes. Those sub-tomograms should not contain $GABA_AR$ particles. Indeed, our classification successfully determined that these sub-tomograms were devoid of $GABA_ARs$, further validating our classification methods.

Randomization in data collection.

The data collection was randomized. We imaged all the synapses that we were able to observe by EM.

Randomization in data analysis.—We selected points on segmented membranes randomly to generate RDRs on the membrane. We selected points on segmented membranes randomly and removed overlapping points (that is, the distance between any two receptors was larger than 7 nm) to generate RDRs* on the membrane. The number of random points was the same as the number of receptors for each synapse. For the randomized data in Extended Data Fig. 9, localization of randomized vesicles was chosen randomly on synaptic membranes. We repeated the randomization ten times for each synapse. The mean number of randomized vesicles inside or outside of the mesophase boundary was used for statistical analysis.

Blinding.—Data collection and analysis were not performed blinded to the conditions of the experiments. All data analyses were performed with automated software using consistent parameters. There was no need to separate the acquired synaptic tomograms into groups for comparison.

Statistical analysis.—Two-tailed Student's t-tests or two-sided Kolmogorov–Smirnov tests were used for two-group comparisons. For all t-tests used in this study, data distributions are provided, and data distribution was assumed to be normal. Original data can be found in the Supplementary Tables and Source Data figures.

Reporting Summary.

Further information on research design is available in the Nature Research Reporting Summary linked to this article.

Data availability

The data that support the findings of this study are available from the corresponding authors upon reasonable request. The density map of $GABA_AR$ and receptor pair have been deposited in the Electron Microscopy Databank (EMDB) under accession numbers EMD-22365 and EMD-22366, respectively. Source data are provided with this paper.

Code availability

The code for random sampling and analysis of sub-tomograms is deposited at https://github.com/procyontao/cryoET-membrane-sampling. The code for simulation of receptor and gephyrin is deposited at https://github.com/alienPQ/Receptors-clustering. Source data are provided with this paper.

Extended Data
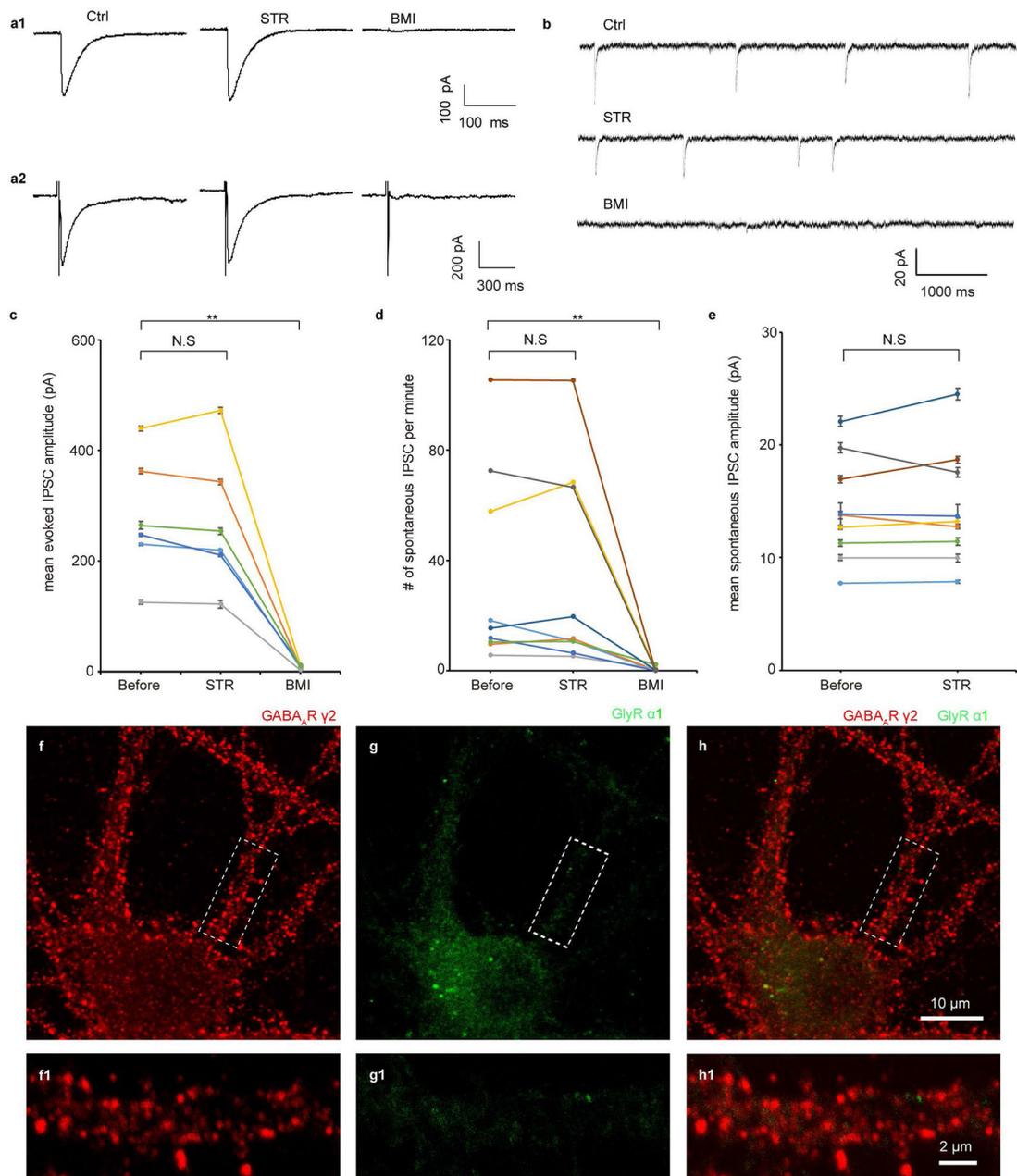
Extended Data Fig. 1 |. Expression of GABA$_A$Rs in cultured hippocampal inhibitory synapses.
a1, Current traces of synaptic IPSCs recorded from a neuron under voltage clamp. A nearby neuron was voltage clamped and stimulated to evoke the responses. **a2**, Current traces of autaptic IPSCs from a stimulated neuron. **b**, Representative recordings of spontaneous IPSCs (sIPSCs). **c**, Application of 1 μM strychnine (STR) did not affect evoked IPSC (eIPSC) amplitudes (N.S, p = 0.43, two-tailed paired t-test), while 20 μM bicuculline methiodide (BMI) could significantly block evoked IPSCs (**, p = 0.003, two-tailed paired t-test). Data are presented as mean values ± SEM. Each line represents an eIPSC (n = 6

neurons). **d**, 1 μM strychnine did not affect the frequency of sIPSCs (N.S, p = 0.90, two-tailed paired t-test), while 20 μM BMI almost totally abolished sIPSCs (*, p = 0.026, two-tailed paired t-test). Each line represents a recorded neuron (n = 8 neurons). **e**, 1 μM strychnine did not affect the amplitude of sIPSCs (N.S, p = 0.71, two-tailed paired t-test, n = 8 neurons). During BMI treatment, sIPSCs were so rare thus not included for comparison. Data are presented as mean values ± SEM. **f**, **g**, Example confocal fluorescent micrographs of cultured neurons with immunostaining of $GABA_A R$ γ2 subunits (red, **f**) and GlyR α1 subunits (green, **g**). **h**, The merged image from **f** and **g**. **f1-h1**, Magnified views of the boxed area in respective images showing putative receptor puncta along with dendrite segments. The experiments in **f-h** were repeated 3 times independently, and 10 neurons were imaged with similar results.
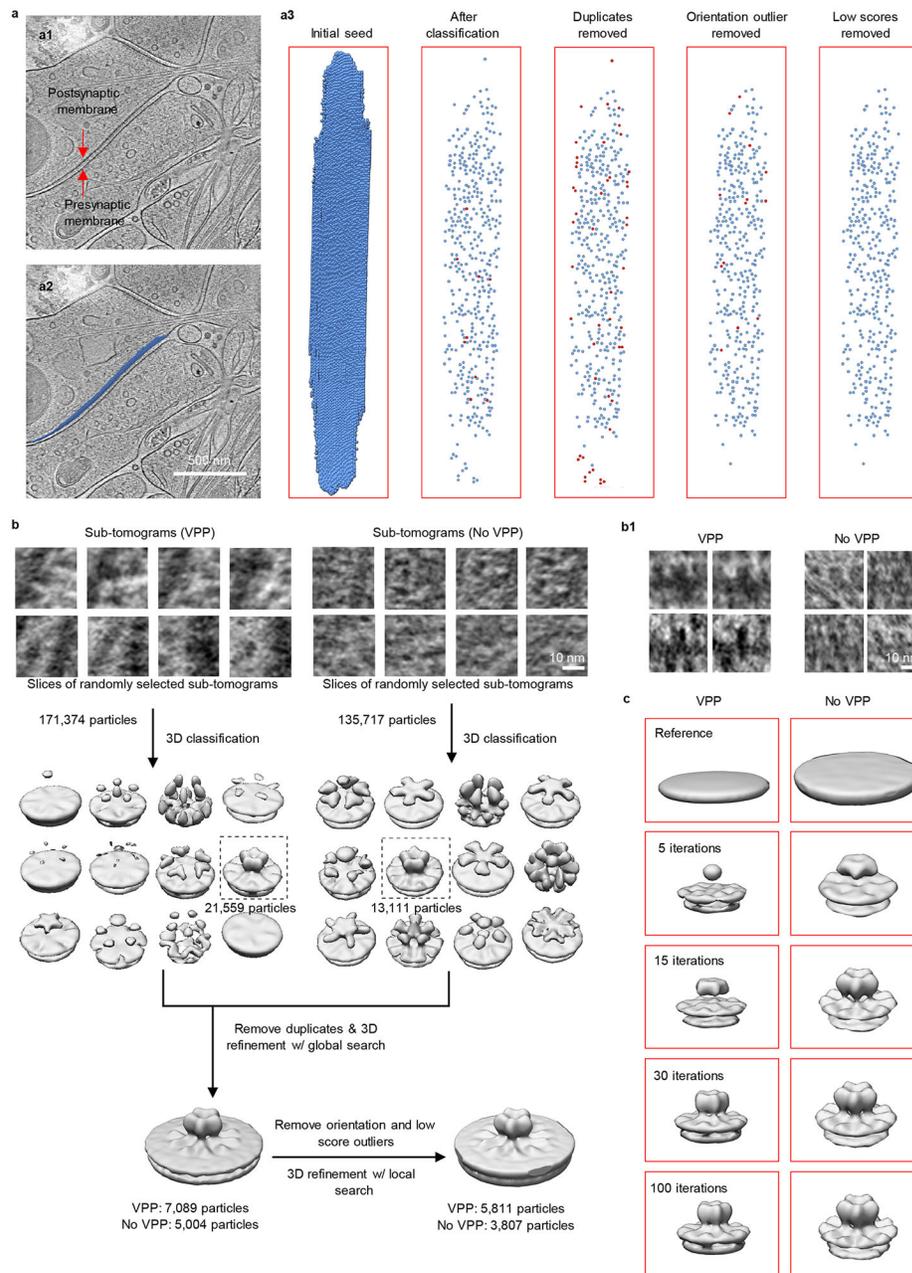
Extended Data Fig. 2 |. Flowchart illustrates identification and sub-tomogram averaging of GABA$_A$R.

a, Steps for identifying GABA$_A$Rs from sampling points. **a1**, Electron tomographic slice of an inhibitory synapse. **a2**, Electron tomographic slice superposed with sampling points on postsynaptic membrane. **a3**, Sampling points after each step. Red points are sampling points that will be discarded in the next step. For **a1-a3**, n = 72 synapses in 70 tomograms. **b**, Classification and refinement of GABA$_A$Rs on postsynaptic membrane. Example 2D slices of sub-tomograms are from 171,374 (left, imaged with VPP) and 135,717 (right, imaged without VPP) sampled sub-tomograms. **b1**, Example 2D slices of aligned sub-tomograms of

GABA$_A$Rs (n = 5,811 sub-tomograms imaged with VPP, n = 3,807 sub-tomograms imaged without VPP). **c**, Structure of GABA$_A$R emerged during iterative classification.
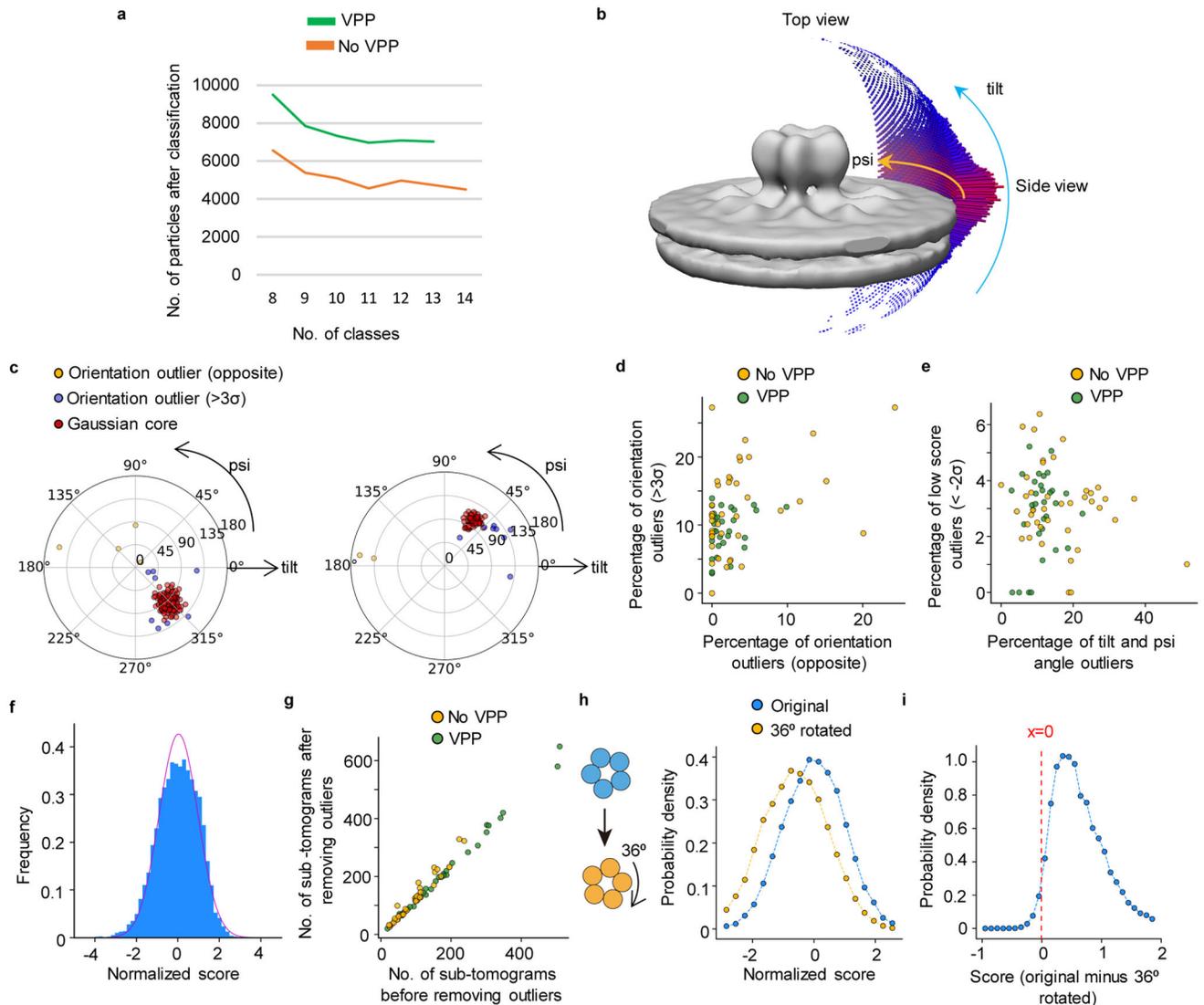
Extended Data Fig. 3 |. Performance estimation of template-free classification and refinement.
a, Number of classified GABA$_A$R sub-tomograms plotted against the number of classes. **b**, Euler (psi and tilt) angles of all sub-tomograms used for the final sub-tomogram averaging. **c**, Distribution of Euler angles for sub-tomograms in two example synapses after first round of refinement. **d**, Percentage of outliers with opposite angles versus percentage of outliers with angles 3σ away from Gaussian core in each synapse. **e**, Percentage of all orientation outliers versus percentage of low score outliers in each synapse. **f**, Frequency distribution of sub-tomogram scores fitted with Gaussian curve (red curve). **g**, Number of sub-tomograms before and after removing both orientation and low score outliers. **h**, Normalized CC score distribution of sub-tomograms comparing with original sub-tomogram average and 36° rotated sub-tomogram average. **i**, Distribution of CC score differences for sub-tomograms comparing with original sub-tomogram average and 36° rotated sub-tomogram average.
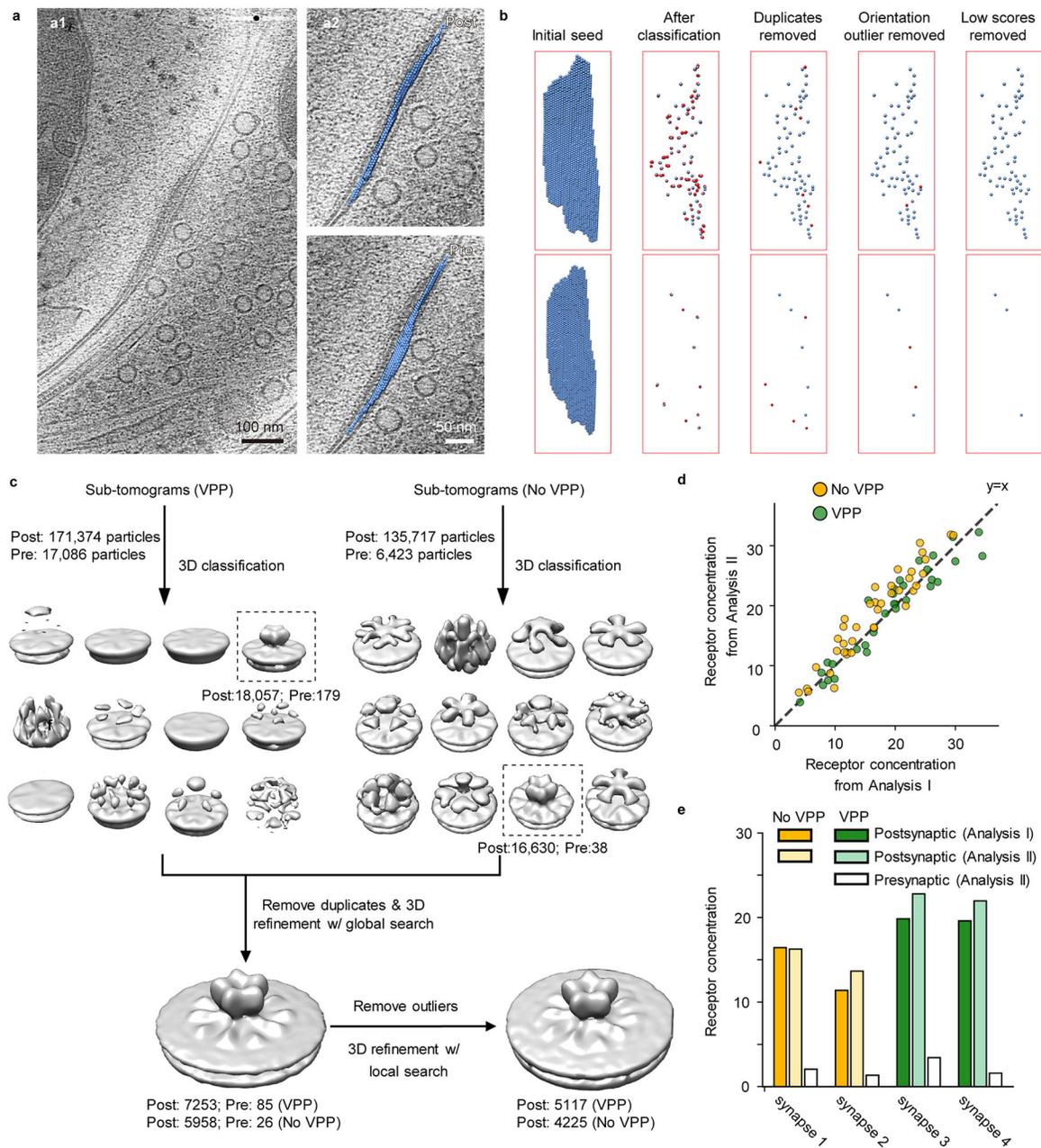
Extended Data Fig. 4 |. Identification of GABA$_A$Rs using sub-tomograms mixed with sub-tomograms on presynaptic membrane.

a, Steps for identifying GABA$_A$Rs from dataset mixed with sub-tomograms on presynaptic membrane. **a1**, Electron tomographic slice of an inhibitory synapse. **a2**, Electron tomographic slices superposed with sampling points on postsynaptic membrane (top) or presynaptic membrane (bottom). **b**, Sub-tomogram sampling points on postsynaptic membrane (top) or presynaptic (bottom) after each step. Red points are sampling points that will be discarded in the next step. For **a** and **b**, n = 72 postsynaptic membranes, and n = 4 presynaptic membranes. **c**, 3D classification and refinement of sub-tomograms on 72 postsynaptic membranes and 4 presynaptic membranes. **d**, Receptor concentration from

Analysis II (analysis of sub-tomograms mixed with presynaptic sub-tomograms) versus receptor concentration from Analysis I (analysis of sub-tomograms without presynaptic sub-tomograms). **e**, Concentration of identified receptors on postsynaptic membranes in Analysis I, Analysis II, and falsely identified receptors on presynaptic membranes in Analysis II for the 4 selected synapses.
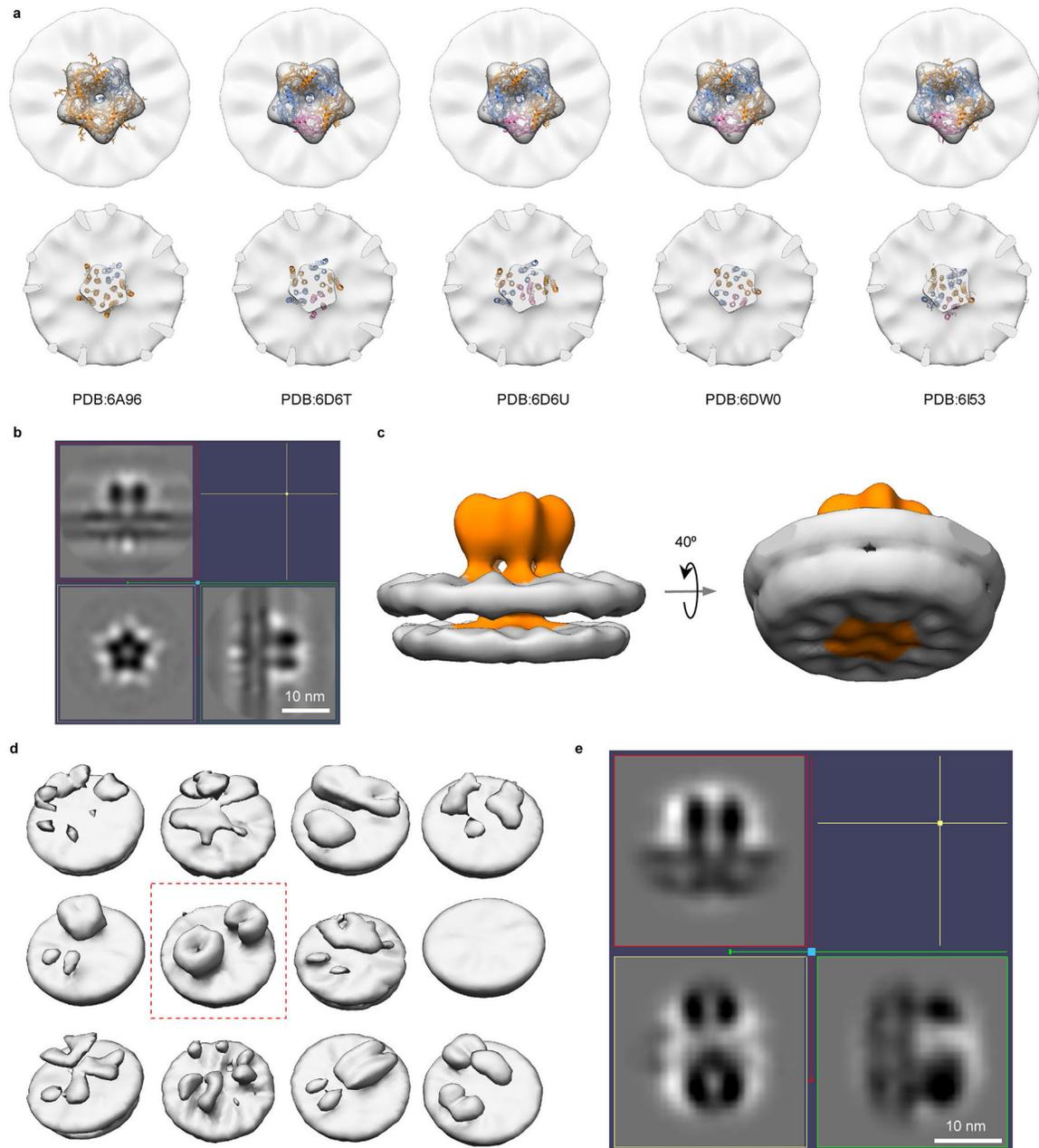
Extended Data Fig. 5 |. Structure features of the sub-tomogram average of GABA$_A$R.
a, Density of the sub-tomogram average fitted with atomic models of different subunit compositions or conformations[26,29-31]. **b**, Orthogonal slice views of sub-tomogram average of GABA$_A$R. **c**, Left: Sub-tomogram average of GABA$_A$R. Orange density is GABA$_A$R

density. Gray density is membrane bilayer. Right: Rotated view of sub-tomogram average of GABA$_A$R displayed at low threshold. **d**, Classification of oversampled sub-tomograms without symmetry. Structures obtained from the 3D classification of VPP data. **e**, Orthogonal slice views of the structure boxed in **d**.
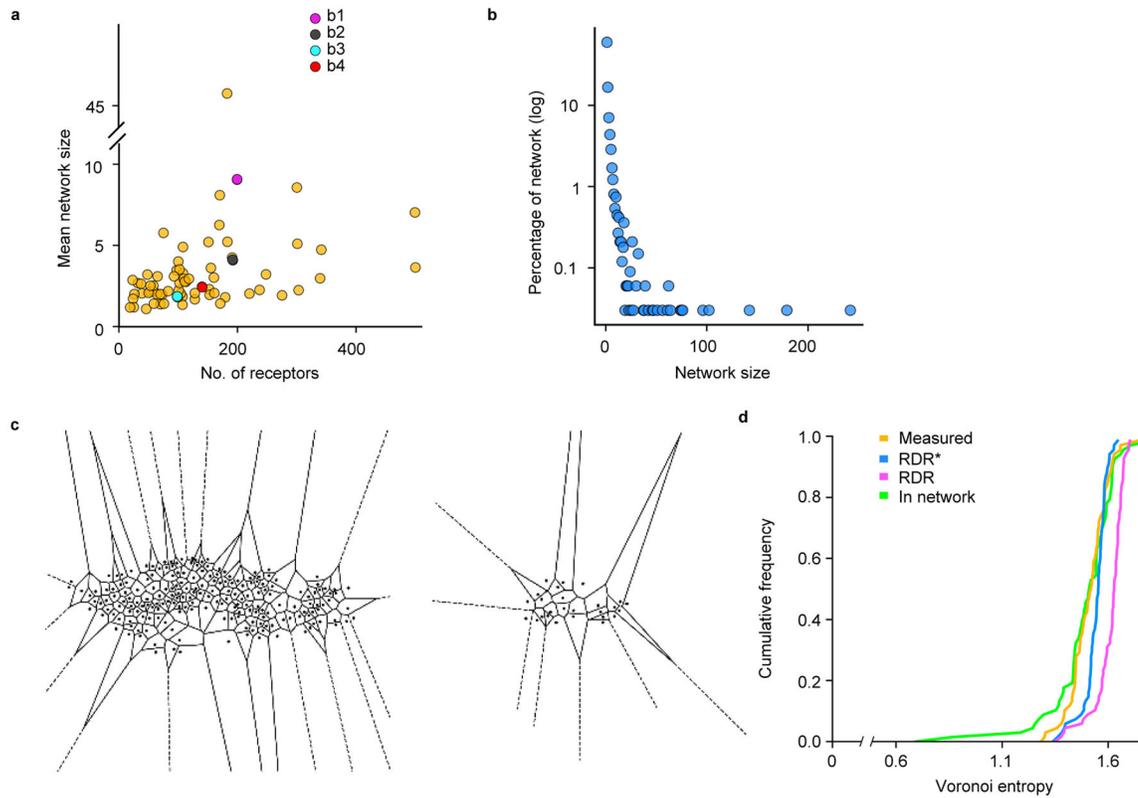
Extended Data Fig. 6 |. Two-dimensional networks of GABA$_A$Rs.
a, Scatter plot of mean network size (number of receptors divided by number of networks) and number of receptors for each synapse. Colored dots (magenta, gray, cyan and red) correspond to the four synapses in Fig. 3b respectively. **b**, Distribution of network size. Y-axis is the plot in logarithm scale. **c**, Examples of Voronoi tessellation of receptors on postsynaptic membranes. Black dots represent the localizations of GABA$_A$Rs. **d**, Cumulative frequency of Voronoi entropy for each synapse. The green line shows the Voronoi entropy of 'networked' receptors.
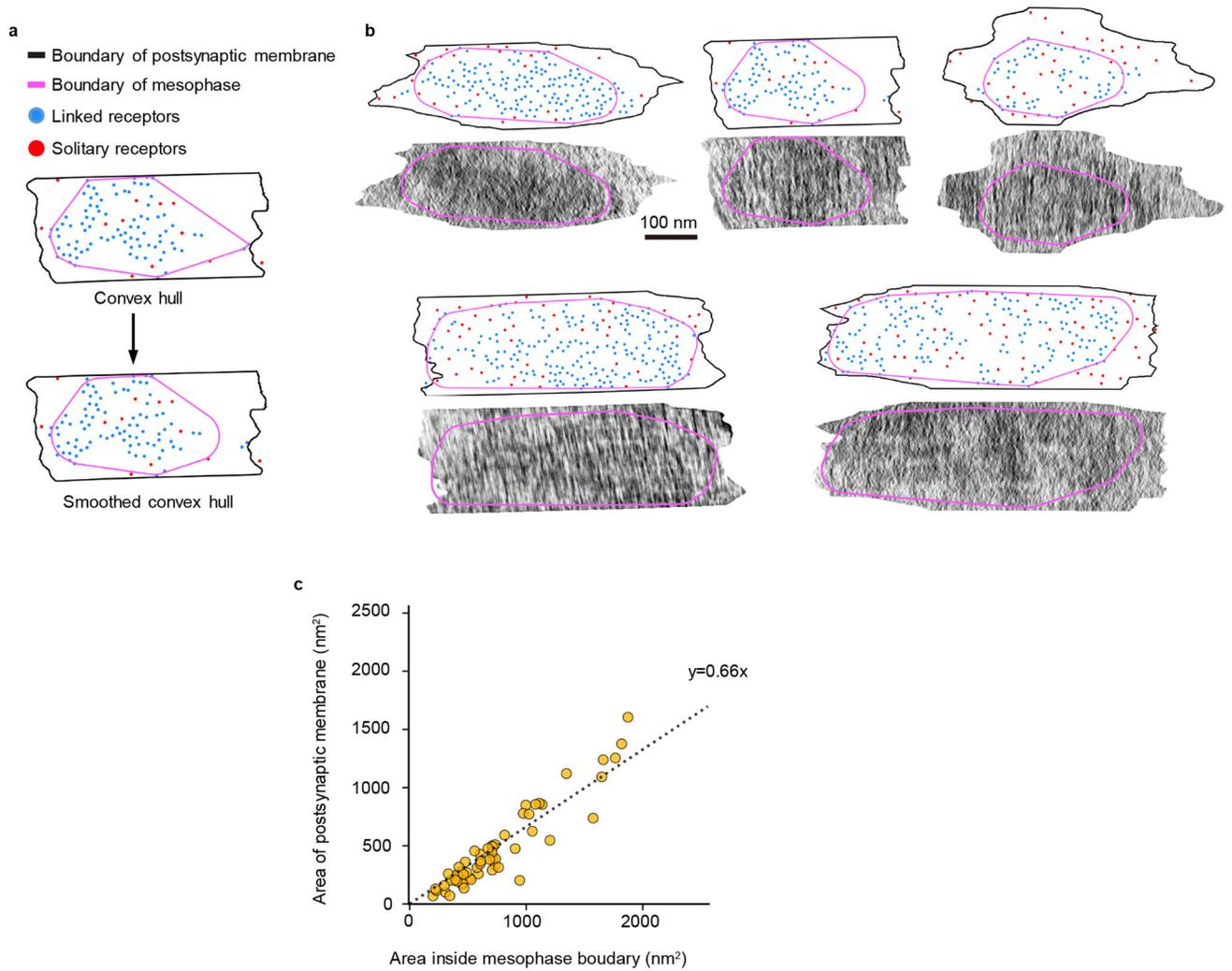
Extended Data Fig. 7 |. Mesophasic assembly of PSD.
a, Example of convex hull and smooth convex hull of linked receptors (n = 58 synapses). **b**, Examples of receptor distribution on the postsynaptic membranes and the corresponding 2D density profiles of scaffolding layer (n = 58 synapses). **c**, Scatter plot of area inside mesophase boundary and area of postsynaptic membrane, fitted with a dashed line.
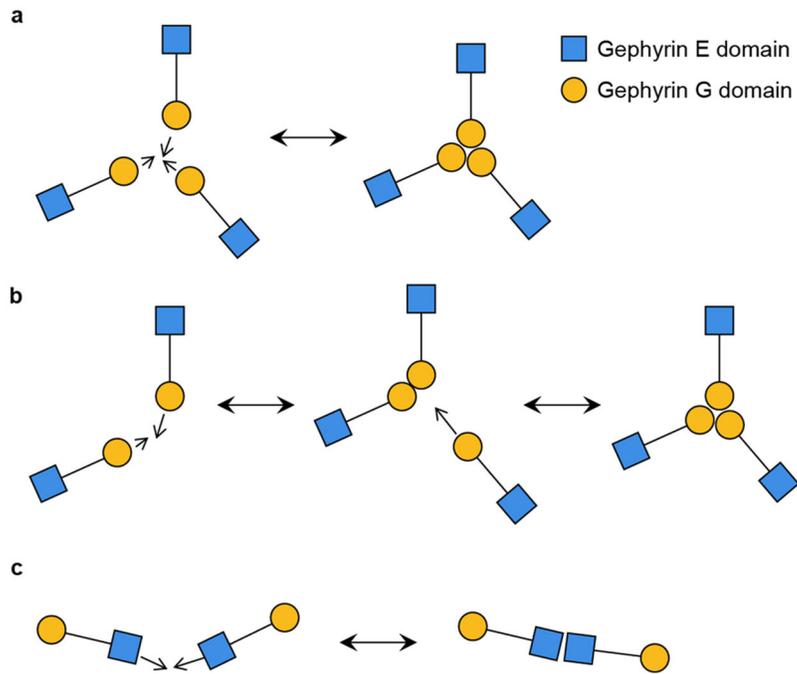
Extended Data Fig. 8 |. Three types of interactions among gephyrin E and G domains in the simulation of gephyrin and GABA$_A$R organization.

a, Direct trimerization of the gephyrin G domains. **b**, Gephyrin G domain trimerization through a dimer intermediate. **c**, Dimerization of gephyrin E domains.
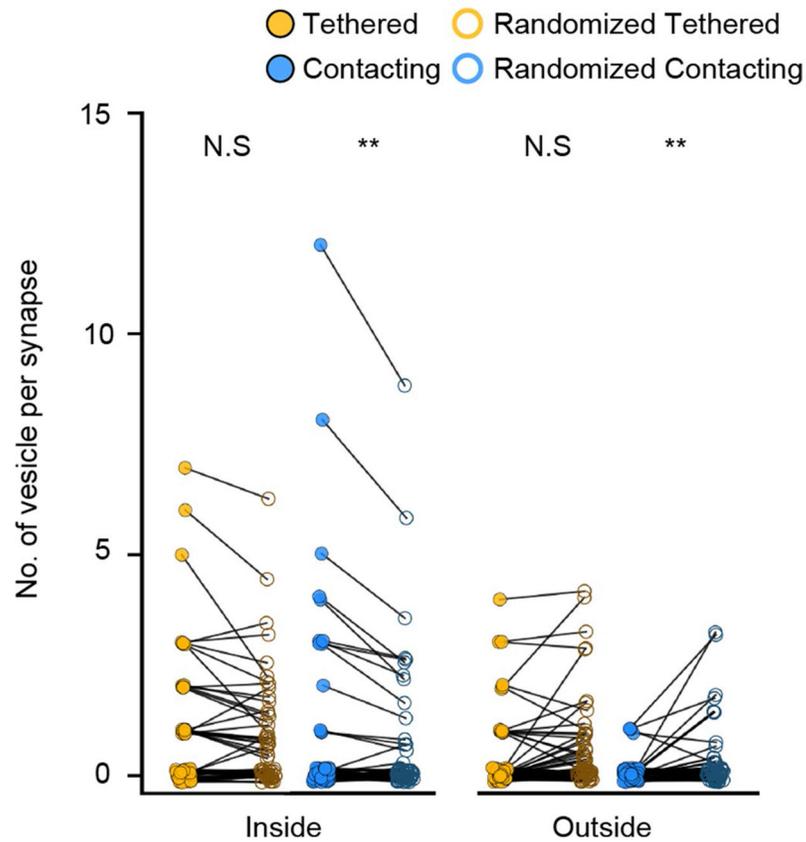
Extended Data Fig. 9 |. Vesicle contacting sites on the presynaptic membrane correlate with mesophasic assembly of GABA$_A$Rs.

Comparison between the number of tethered or contacting vesicles inside or outside of mesophase boundary with the corresponding number based on randomized vesicle distribution within the whole synapse (n = 58 synapses). For both inside and outside mesophase boundary, N.S, p = 0.20; **, p = 0.005, two-tailed paired t-test.
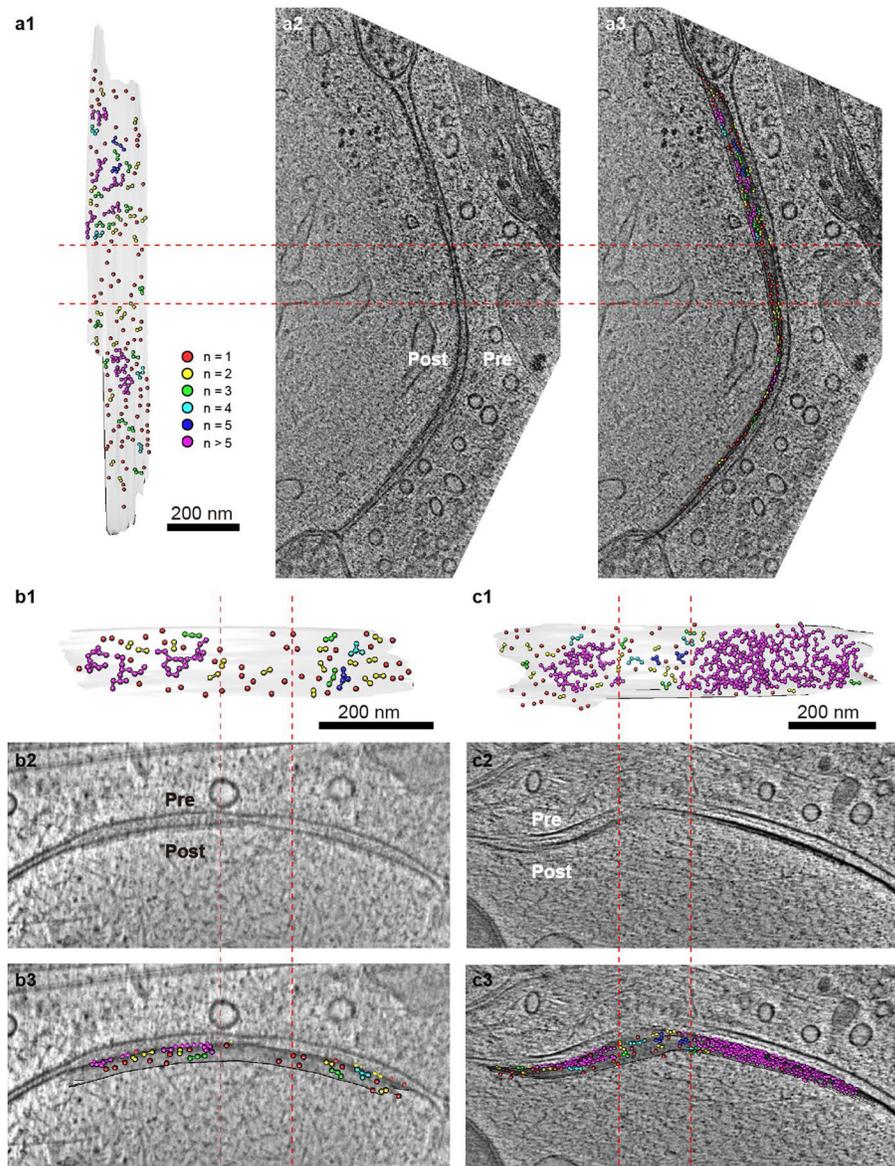
Extended Data Fig. 10 |. Synapses with two discretely separated receptor assemblies.
Synapses had narrow synaptic clefts (n = 2 synapses) (**a**, **b**) or deformed synaptic
membranes (n = 1 synapse) (**c**). **a1-c1**, *En face* views of GABA$_A$Rs (colored dots) on the
postsynaptic membrane (transparent gray). **a2-c2**, Tomographic slices of the respective
synapses. **a3-c3**, Side views superposed with the tomographic slices. Color indicates
network size (n, the number of receptors in a network). Paired red dashed lines indicate the
gap between two receptor assemblies and the corresponding synaptic cleft area.

Supplementary Material

Refer to Web version on PubMed Central for supplementary material.

Acknowledgements

References

1. Eccles JC Developing concepts of the synapses. J. Neurosci 10, 3769–3781 (1990). [PubMed: 1980129]

2. Sudhof TC & Malenka RC Understanding synapses: past, present, and future. Neuron 60, 469–476 (2008). [PubMed: 18995821]

3. Mayford M, Siegelbaum SA & Kandel ER Synapses and memory storage. Cold Spring Harbor Perspect. Biol 4, a005751 (2012).

4. Sheng M, Sabatini BL & Sudhof TC Synapses and Alzheimer's disease. Cold Spring Harbor Perspect. Biol 4, a005777 (2012).

5. Dosemeci A, Weinberg RJ, Reese TS & Tao-Cheng JH The postsynaptic density: there is more than meets the eye. Front. Synaptic Neurosci 8, 23 (2016). [PubMed: 27594834]

6. Liu YT, Tao CL, Lau PM, Zhou ZH & Bi GQ Postsynaptic protein organization revealed by electron microscopy. Curr. Opin. Struct. Biol 54, 152–160 (2019). [PubMed: 30904821]

7. Tao CL et al. Differentiation and characterization of excitatory and inhibitory synapses by cryo-electron tomography and correlative microscopy. J. Neurosci 38, 1493–1510 (2018). [PubMed: 29311144]

8. Valtschanoff JG & Weinberg RJ Laminar organization of the NMDA receptor complex within the postsynaptic density. J. Neurosci 21, 1211–1217 (2001). [PubMed: 11160391]

9. Tang AH et al. A trans-synaptic nanocolumn aligns neurotransmitter release to receptors. Nature 536, 210–214 (2016). [PubMed: 27462810]

10. Pennacchietti F et al. Nanoscale molecular reorganization of the inhibitory postsynaptic density is a determinant of GABAergic synaptic potentiation. J. Neurosci 37, 1747–1756 (2017). [PubMed: 28073939]

11. Mele M, Leal G & Duarte CB Role of GABA$_A$ R trafficking in the plasticity of inhibitory synapses. J. Neurochem 139, 997–1018 (2016). [PubMed: 27424566]

12. Penn AC et al. Hippocampal LTP and contextual learning require surface diffusion of AMPA receptors. Nature 549, 384–388 (2017). [PubMed: 28902836]

13. Chen X et al. Organization of the core structure of the postsynaptic density. Proc. Natl Acad. Sci. USA 105, 4453–4458 (2008). [PubMed: 18326622]

14. DeGiorgis JA, Galbraith JA, Dosemeci A, Chen X & Reese TS Distribution of the scaffolding proteins PSD-95, PSD-93, and SAP97 in isolated PSDs. Brain Cell Biol. 35, 239–250 (2006). [PubMed: 18392731]

15. Sheng M & Kim E The postsynaptic organization of synapses. Cold Spring Harbor Perspect. Biol 3, a005678 (2011).

16. Nair D et al. Super-resolution imaging reveals that AMPA receptors inside synapses are dynamically organized in nanodomains regulated by PSD95. J. Neurosci 33, 13204–13224 (2013). [PubMed: 23926273]

17. MacGillavry HD, Song Y, Raghavachari S & Blanpied TA Nanoscale scaffolding domains within the postsynaptic density concentrate synaptic AMPA receptors. Neuron 78, 615–622 (2013). [PubMed: 23719161]

18. Crosby KC et al. Nanoscale subsynaptic domains underlie the organization of the inhibitory synapse. Cell Rep. 26, 3284 (2019). [PubMed: 30893601]

19. Zeng M et al. Reconstituted postsynaptic density as a molecular platform for understanding synapse formation and plasticity. Cell 174, 1172–1187 (2018). [PubMed: 30078712]

20. Zeng M et al. Phase transition in postsynaptic densities underlies formation of synaptic complexes and synaptic plasticity. Cell 166, 1163–1175 (2016). [PubMed: 27565345]

21. Specht CG et al. Quantitative nanoscopy of inhibitory synapses: counting gephyrin molecules and receptor binding sites. Neuron 79, 308–321 (2013). [PubMed: 23889935]

22. Miller PS & Aricescu AR Crystal structure of a human GABA$_A$ receptor. Nature 512, 270–275 (2014). [PubMed: 24909990]

23. Loh KH et al. Proteomic analysis of unbounded cellular compartments: synaptic clefts. Cell 166, 1295–1307 (2016). [PubMed: 27565350]

24. Nusser Z, Hajos N, Somogyi P & Mody I Increased number of synaptic GABA$_A$ receptors underlies potentiation at hippocampal inhibitory synapses. Nature 395, 172–177 (1998). [PubMed: 9744275]

25. Scheres SH RELION: implementation of a Bayesian approach to cryo-EM structure determination. J. Struct. Biol 180, 519–530 (2012). [PubMed: 23000701]

26. Zhu S et al. Structure of a human synaptic GABA$_A$ receptor. Nature 559, 67–72 (2018). [PubMed: 29950725]

27. Han W et al. Shisa7 is a GABA$_A$ receptor auxiliary subunit controlling benzodiazepine actions. Science 366, 246–250 (2019). [PubMed: 31601770]

28. Yamasaki T, Hoyos-Ramirez E, Martenson JS, Morimoto-Tomita M & Tomita S GARLH family proteins stabilize GABA$_A$ receptors at synapses. Neuron 93, 1138–1152 (2017). [PubMed: 28279354]

29. Liu S et al. Cryo-EM structure of the human α5β3 GABA$_A$ receptor. Cell Res. 28, 958–961 (2018). [PubMed: 30140029]

30. Phulera S et al. Cryo-EM structure of the benzodiazepine-sensitive α1β1γ2S tri-heteromeric GABA$_A$ receptor in complex with GABA. eLife 7, e39383 (2018). [PubMed: 30044221]

31. Laverty D et al. Cryo-EM structure of the human α1β3γ2 GABA$_A$ receptor in a lipid bilayer. Nature 565, 516–520 (2019). [PubMed: 30602789]

32. Blanpied TA, Kerr JM & Ehlers MD Structural plasticity with preserved topology in the postsynaptic protein network. Proc. Natl Acad. Sci. USA 105, 12587–12592 (2008). [PubMed: 18723686]

33. Bak P, Tang C & Wiesenfeld K Self-organized criticality: an explanation of the 1/fnoise. Phys. Rev. Lett 59, 381–384 (1987). [PubMed: 10035754]

34. Bormashenko E et al. Characterization of self-assembled 2D patterns with Voronoi entropy. Entropy 20, 956 (2018).

35. Limaye AV, Narhe RD, Dhote AM & Ogale SB Evidence for convective effects in breath figure formation on volatile fluid surfaces. Phys. Rev. Lett 76, 3762–3765 (1996). [PubMed: 10061103]

36. Zuber B & Unwin N Structure and superorganization of acetylcholine receptor-rapsyn complexes. Proc. Natl Acad. Sci. USA 110, 10622–10627 (2013). [PubMed: 23754381]

37. Heuser JE & Salpeter SR Organization of acetylcholine receptors in quick-frozen, deep-etched, and rotary-replicated Torpedo postsynaptic membrane. J. Cell Biol 82, 150–173 (1979). [PubMed: 479296]

38. Sola M et al. Structural basis of dynamic glycine receptor clustering by gephyrin. EMBO J. 23, 2510–2519 (2004). [PubMed: 15201864]

39. Saiyed T et al. Molecular basis of gephyrin clustering at inhibitory synapses - role of G- and E-domain interactions. J. Biol. Chem 282, 5625–5632 (2007). [PubMed: 17182610]

40. Maric HM et al. Molecular basis of the alternative recruitment of GABA$_A$ versus glycine receptors through gephyrin. Nat. Commun 5, 5767 (2014). [PubMed: 25531214]

41. Fernandez-Busnadiego R et al. Quantitative analysis of the native presynaptic cytomatrix by cryoelectron tomography. J. Cell Biol 188, 145–156 (2010). [PubMed: 20065095]

42. Zuber B & Lucic V Molecular architecture of the presynaptic terminal. Curr. Opin. Struct. Biol 54, 129–138 (2019). [PubMed: 30925443]

43. Levi S, Logan SM, Tovar KR & Craig AM Gephyrin is critical for glycine receptor clustering but not for the formation of functional GABAergic synapses in hippocampal neurons. J. Neurosci 24, 207–217 (2004). [PubMed: 14715953]

44. Tretter V et al. Gephyrin, the enigmatic organizer at GABAergic synapses. Front. Cell. Neurosci 6, 23 (2012). [PubMed: 22615685]

45. Tao CL, Liu YT, Zhou ZH, Lau PM & Bi GQ Accumulation of dense core vesicles in hippocampal synapses following chronic inactivity. Front. Neuroanat 12, 48 (2018). [PubMed: 29942253]

46. Sutton MA et al. Miniature neurotransmission stabilizes synaptic function via tonic suppression of local dendritic protein synthesis. Cell 125, 785–799 (2006). [PubMed: 16713568]

47. Sun R et al. An efficient protocol of cryo-correlative light and electron microscopy for the study of neuronal synapses. Biophysics Rep. 5, 111–122 (2019).

48. Kremer JR, Mastronarde DN & McIntosh JR Computer visualization of three-dimensional image data using IMOD. J. Struct. Biol 116, 71–76 (1996). [PubMed: 8742726]

49. Mastronarde DN Automated electron microscope tomography using robust prediction of specimen movements. J. Struct. Biol 152, 36–51 (2005). [PubMed: 16182563]

50. Li XM et al. Electron counting and beam-induced motion correction enable near-atomic-resolution single-particle cryo-EM. Nat. Methods 10, 584 (2013). [PubMed: 23644547]

51. Rohou A & Grigorieff N CTFFIND4: fast and accurate defocus estimation from electron micrographs. J. Struct. Biol 192, 216–221 (2015). [PubMed: 26278980]

52. Turonova B, Schur FKM, Wan W & Briggs JAG Efficient 3D-CTF correction for cryo-electron tomography using NovaCTF improves subtomogram averaging resolution to 3.4Å. J. Struct. Biol 199, 187–195 (2017). [PubMed: 28743638]

53. Pettersen EF et al. UCSF Chimera—a visualization system for exploratory research and analysis. J. Comput. Chem 25, 1605–1612 (2004). [PubMed: 15264254]

54. Hrabe T et al. PyTom: a Python-based toolbox for localization of macromolecules in cryo-electron tomograms and subtomogram analysis. J. Struct. Biol 178, 177–188 (2012). [PubMed: 22193517]

55. Mattei S, Glass B, Hagen WJH, Krausslich HG & Briggs JAG The structure and flexibility of conical HIV-1 capsids determined within intact virions. Science 354, 1434–1437 (2016). [PubMed: 27980210]

56. Navarro PP, Stahlberg H & Castano-Diez D Protocols for subtomogram averaging of membrane proteins in the dynamo software package. Front. Mol. Biosci 5, 82 (2018). [PubMed: 30234127]

57. Zivanov J et al. New tools for automated high-resolution cryo-EM structure determination in RELION-3. eLife 7, e42166 (2018). [PubMed: 30412051]

58. Rosenthal PB & Henderson R Optimal determination of particle orientation, absolute hand, and contrast loss in single-particle electron cryomicroscopy. J. Mol. Biol 333, 721–745 (2003). [PubMed: 14568533]
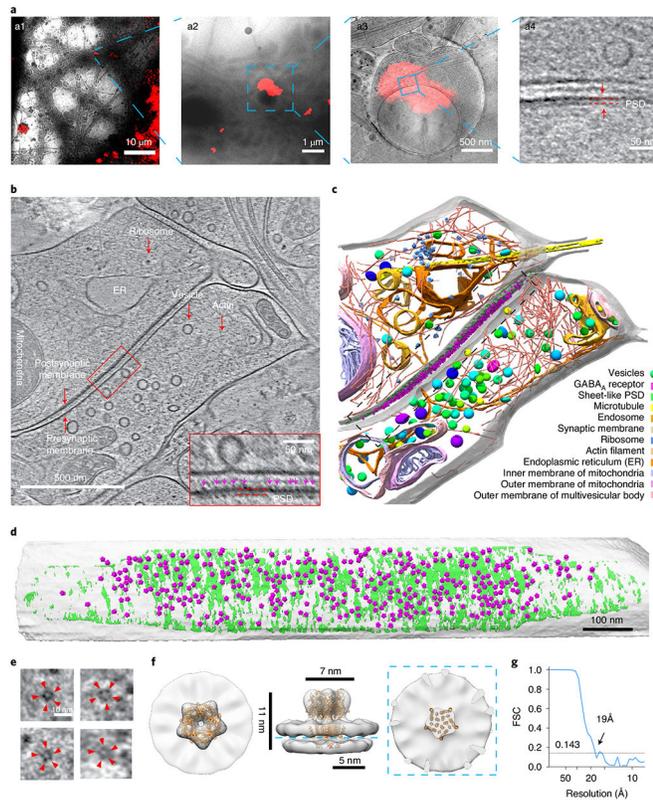
Fig. 1 |. Identification and in situ structure of GABA$_A$R in inhibitory synapses.
a, Identification of inhibitory synapses with cryo-correlative LM and EM (*n* = 8 synapses).
a1, Low-magnification EM image superposed with fluorescence image of gephyrin-mCherry. **a2**, Zoomed-in view of **a1**. **a3**, Electron tomographic slice superposed with fluorescence puncta. **a4**, Zoomed-in view of **a3** showing thin, sheet-like PSD. **b**, A tomographic slice of an inhibitory synapse (*n* = 72 synapses observed in 70 tomograms). Various subcellular components are labeled on the image. Inset: zoomed-in view showing receptor densities (magenta arrowheads). **c**, 3D rendering of synaptic structures in the tomogram shown in **b**. **d**, Front view of boxed area in **c**, showing GABA$_A$Rs (purple) and densities of the scaffolding protein layer (green) on the postsynaptic membrane (transparent gray). **e**, Example tomographic slices of individual GABA$_A$R in top view (*n* = 9,618 GABA$_A$R sub-tomograms). Red arrowheads showing five blobs of GABA$_A$R density. **f**, Sub-tomogram average of GABA$_A$R fitted with crystal structure (orange ribbons)[22]. **g**, Fourier shell correlation of the GABA$_A$R sub-tomogram average. FSC, Fourier shell correlation.
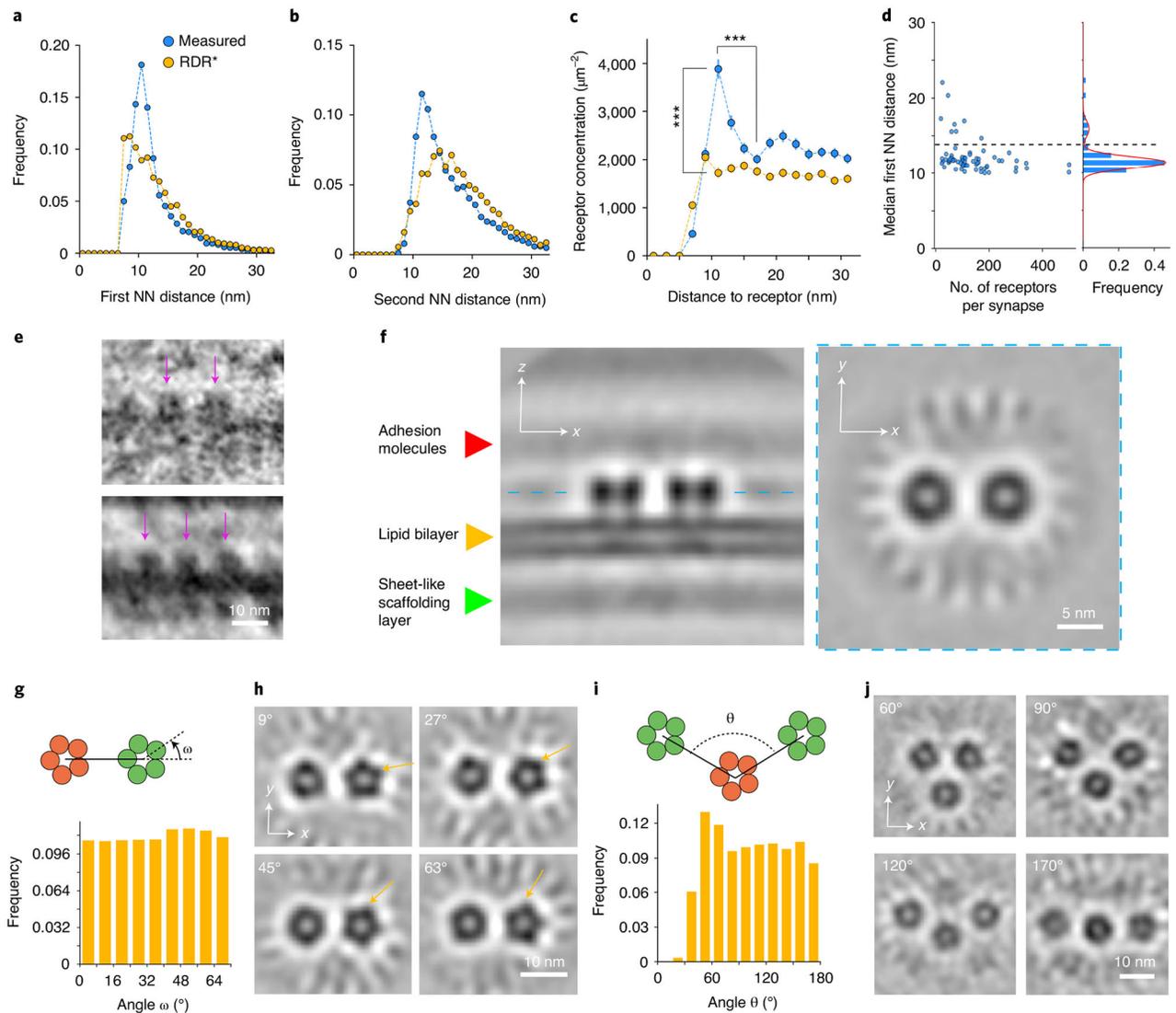
Fig. 2 |. GABA_AR super-complexes.

a,b, The first (**a**) and second (**b**) NN distances distribution of measured receptors (Measured) and a set of simulated receptors that are RDRs* (that is, the distance between any two receptors is larger than 7 nm). $n = 9{,}531$ receptors (**a** and **b**), two-sample, two-sided Kolmogorov-Smirnov tests (**a** and **b**), ***$P = 2.72 \times 10^{-53}$ (**a**) and ***$P = 4.20 \times 10^{-109}$ (**b**). **c**, Mean receptor concentration as a function of distance to a GABA_AR. $n = 70$ synapses, two-tailed, two-sample t-test, ***$P = 1.52 \times 10^{-14}$ for measured receptor concentration versus that of RDR* at 11-nm distance; ***$P = 4.03 \times 10^{-13}$ for receptor concentration at 11 nm verses that at 17 nm. Data are presented as mean values ± s.e.m. **d**, Left: scatter plot of the number of receptors versus the median first NN distance of each synapse. Right: frequency distribution of median first NN distance, fitted with two Gaussian distributions (red curve). The dashed line shows the lowest point between the two peaks. **e**, Examples of receptor pairs and triplets from original tomograms ($n = 16{,}234$ receptor pair sub-tomograms). Arrows point to receptors. **f**, Orthogonal slice views of the sub-tomogram average of receptor pairs

(n = 16,234 receptor pair sub-tomograms). **g,i**, The distribution of relative rotation angles ω (**g**) and θ (**i**), as defined in respective diagrams. n = 16,234 receptor pairs (**g**) and n = 14,098 receptor triplets (**i**). **h,j**, 2D central slices of sub-tomogram averages of receptor pairs with different ω (**h**) and receptor triplets with different θ (**j**). Four panels in **h** are the averaged images of 3,883 (top left), 3,957 (top right), 4,199 (bottom left) and 4,195 (bottom left) sub-tomograms, respectively. Four panels in **j** are the averaged images of 2,428 (top left), 1,772 (top right), 1,937 (bottom left) and 1,714 (bottom left) sub-tomograms, respectively. Statistics data for **a**-**c** can be found in Source Data.
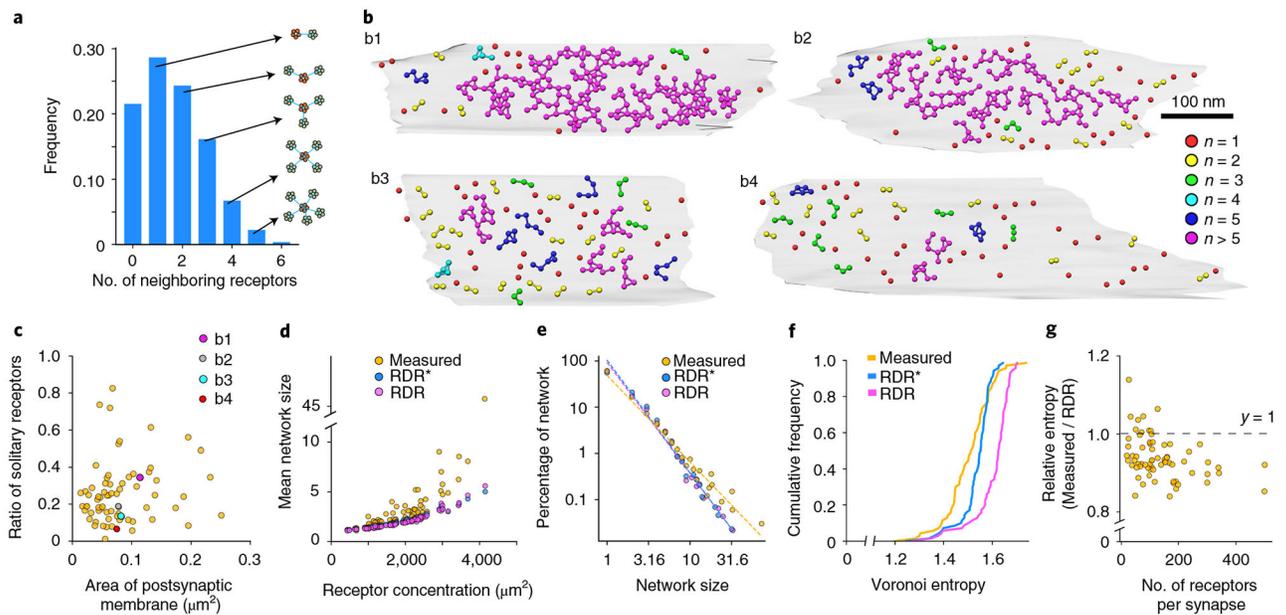
Fig. 3 |. 2D networks of GABA$_A$Rs.
a, Distribution of the number of receptors with different numbers of 11-nm neighbors (n = 9,531 receptors). **b**, Four examples from 70 synapses (**b1**-**b4**) of receptor network organization on the postsynaptic membrane. Colors indicate network size (n, the number of receptors in a network). **c**, Scatter plot of the ratio of solitary receptors versus the area of postsynaptic membrane for each synapse. Colored dots (magenta, gray, cyan and red) correspond to synapses in **b**. **d**, Scatter plot of mean network size versus receptor concentration for measured receptors (Measured), RDRs and RDRs*. **e**, Power law distribution of network size in log-log plot. **f**, Cumulative frequency of Voronoi entropy for each synapse. n = 70 synapses, $P = 1.86 \times 10^{-3}$ (RDR* versus RDR), $P = 6.81 \times 10^{-11}$ (RDR* versus Measured), two-sample, two-sided Kolmogorov-Smirnov tests. **g**, Scatter plot of relative entropy (defined as Measured/RDR) versus the number of receptors for each synapse.
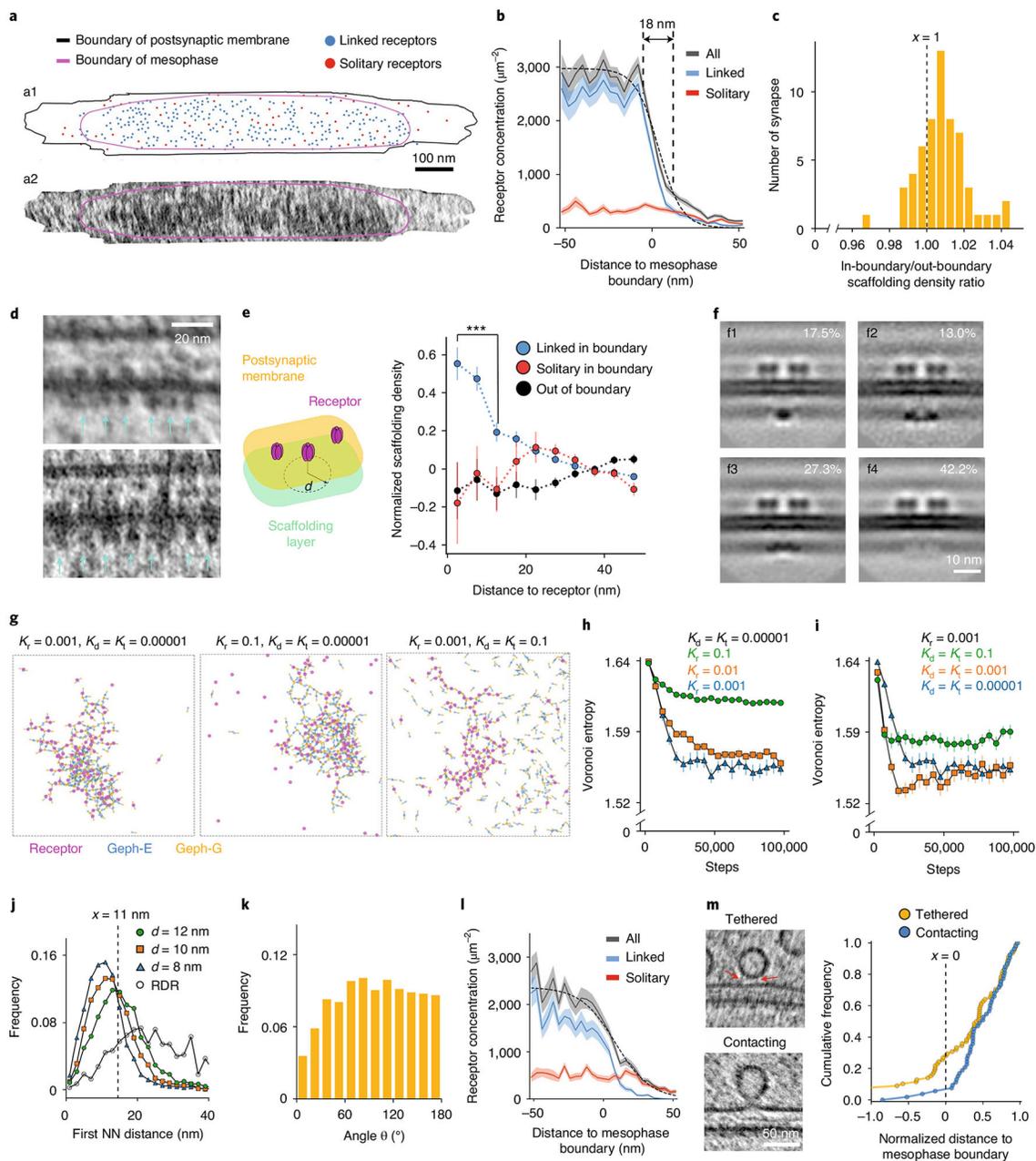
Fig. 4 |. Mesophasic assembly of inhibitory PSD.

a, Examples of receptor distribution ($n = 58$ synapses) on the postsynaptic membrane (**a1**) and the corresponding density projection of the scaffolding layer (**a2**). **b**, Receptor concentration as a function of distance to the mesophase boundary ($n = 58$ synapses). The dashed curve is a sigmoid function fitted with the black curve. Data are presented as mean values (the curves) ± s.e.m. (the light shadow). Vertical dashed lines, 80%–20% width of the sigmoid function. **c**, Histogram of the number of synapses with various ratios of average scaffolding density inside the mesophase boundary to that outside the boundary. **d**, Example of interactions between receptors and scaffolding proteins ($n = 58$ synapses). Cyan arrows indicate the image density of scaffolding proteins interacting with GABA$_A$Rs. **e**, Left:

diagram showing relative positions of scaffolding layer and receptors, with d representing distance to the projection of receptor in the scaffolding layer. Right: normalized image density of the scaffolding layer as a function of d ($n = 6,291$ linked receptors inside the phase boundary, $n = 984$ solidary receptors inside the phase boundary and $n = 1,785$ receptors outside the phase boundary). ***$P = 2.81 \times 10^{-4}$, two-tailed, two-sample t-test. Data are presented as mean values ± s.e.m. **f**, 3D classification showing four types of interactions among scaffolding densities and receptor pairs. The numbers on the top right of each panel show the percentage of particles in each class. Four panels in **f** are the 2D slices of 3D averaged images of 1,786 (top left), 1,330 (top right), 2,794 (bottom left) and 4,312 (bottom left) sub-tomograms. **g**, Examples of simulated GABA$_A$Rs and gephyrin molecules organization at equilibrium state (after 100,000 steps of random walk). Magenta, blue and orange dots represent locations of GABA$_A$Rs, gephyrin E domains and gephyrin G domains, respectively. Short black lines are linkers between the two domains. Dashed lines are boundaries of simulation (500 nm×500 nm). Parameters of simulations are shown on the top of each panel. K_r, off rate of receptor; K_d, off rate of gephyrin E domain dimerization; K_t, off rate of G domain trimerization. **h-i**, Voronoi entropy of receptor distribution as simulation time progresses. Parameters of simulations are shown on each panel. For each line, $n = 28$ simulated synapses. Data are presented as mean values ± s.e.m. **j**, NN distance distribution of receptors simulated with different lengths of gephyrin. d, the length of gephyrin in each simulation ($K_r = 0.001$, $K_t = K_d = 0.00001$, step = 100,000). **k**, The distribution of relative rotation angles θ for receptor triplets in simulation. $n = 5,007$ receptor triplets from simulated synapses ($K_r = 0.001$, $K_t = K_d = 0.00001$, step = 100,000), as defined in Fig. 2i. **l**, Receptor concentration as a function of distance to the mesophase boundary of simulated receptor distribution. For each line, $n = 28$ simulated synapses. $K_r = 0.001$, $K_t = K_d = 0.00001$, step=100,000. The dashed curve is a sigmoid function fitted with the black curve. Light shadow, s.e.m. **m**, Left: example tomographic slices of tethered and contacting vesicles. Red arrows indicate rod-like tethers. Right: cumulative frequency of normalized distance from vesicles to mesophase boundary. A vesicle with normalized distance of 1 is at the center of the mesophasic condensate, whereas a vesicle with normalized distance of 0 is on the mesophase boundary. $n = 81$ for tethered vesicles; $n = 54$ for contacting vesicles. The distributions of the two vesicle populations are significantly different ($P = 0.013$, two-sample, two-tailed t-test). Statistics data for **b** and **e** can be found in Source Data.